

**A MINIMUM-BENDING-ENERGY NEEDLE MODEL
FOR CLOSED-LOOP LOCALIZATION DURING
IMAGE-GUIDED INSERTION**

by

Joseph Schornak

A Thesis submitted to the Faculty of the
WORCESTER POLYTECHNIC INSTITUTE
in partial fulfillment of the requirements for the
Degree of Master of Science in Robotics Engineering

Worcester, Massachusetts

May, 2018

© Joseph Schornak 2018

All rights reserved

Approved by:

Prof. Gregory S. Fischer, Advisor
Worcester Polytechnic Institute

Prof. Loris Fichera, Committee Member
Worcester Polytechnic Institute

Prof. Jie Fu, Committee Member
Worcester Polytechnic Institute

Abstract

Accurate needle placement is critical to the success of needle-based interventions. Needle deflection due to tissue non-homogeneity and dynamic forces results in targeting error, potentially requiring repeated insertions. Real-time imaging enables closed-loop control of the needle during insertion, improving insertion accuracy. The needle localization algorithm proposed in this thesis models the needle as a parametric polynomial equation optimized to minimize beam bending energy relative to a set of observed needle coordinates. Simulated insertions using an MRI dataset show that the minimum bending energy model allows planning of subsequent imaging planes to capture the moving needle while estimating the shape of the needle with low error.

Acknowledgments

Extensive thanks to my thesis advisor Prof. Gregory Fischer and my committee members, Prof. Loris Fichera and Prof. Jie Fu.

I really appreciate the help and support of the other students in the WPI AIM Lab: Anna Novoseltseva, Marek Wartenberg, Katie Gandomi, Paulo Carvalho, Chris Nycz, Chris Bove, and Nirav Patel.

Dedication

This thesis is dedicated to my grandfather, Dr. Joseph Ravin M.D., who wanted to see what I would become.

Contents

Abstract	iii
Acknowledgments	iv
List of Figures	ix
1 Introduction	1
1.1 Motivation	1
1.2 Problem Formulation	3
1.3 Thesis Contributions	4
1.3.1 Minimum Bending Energy Model	4
1.3.2 Needle Localization Algorithm	4
1.3.3 MRI Data Collection	5
1.3.4 Slicer Module	5
1.4 MRI Physics	5
1.5 Tissue Phantoms	7
2 Review of Previous Work	8

2.1	Needle Geometry	8
2.2	Needle Modeling	9
2.2.1	Non-Holonomic Kinematics	10
2.2.2	Finite Element Models	11
2.2.3	Mechanical Models	12
2.3	Needle Steering	13
2.4	Needle Localization	16
2.4.1	Coronal and Sagittal Plane Imaging	17
2.4.2	Transverse Plane Imaging	18
2.4.3	3D Imaging	19
2.4.4	Other Techniques	20
3	Needle Model	22
3.1	Assumptions and Definitions	24
3.2	Beam Bending Energy	26
3.3	Parametric Polynomial Space Curves	27
3.4	Curve Fitting	29
3.4.1	Cost Function	29
3.4.2	Constraints	30
3.5	Software Implementation	31
4	Needle Localization in MR Images	35

4.1	Software Architecture	35
4.1.1	Simulated MRI Scanner	35
4.1.2	Needle Tracking Module	36
4.2	Experiment	36
4.2.1	MRI Data Collection	38
4.2.2	Needle Localization	38
4.3	Results	39
4.3.1	Needle Localization at a Single Timestep	40
4.3.2	Needle Localization at Sequential Timesteps	41
5	Discussion and Conclusion	48
5.1	Discussion	48
5.1.1	MRI Experiment	48
5.1.2	Needle Model	50
5.2	Future Work	51
5.3	Conclusion	51
	References	53

List of Figures

1.1	A manual MRI-guided biopsy in progress (from Tokuda, 2012).	2
1.2	MRI scan of a gelatin tissue phantom undergoing needle insertion. The needle enters the phantom at the right of the image. Note the artifact around the needle tip.	6
2.1	Free-body diagram depicting forces acting on an asymmetric beveled needle tip during insertion into an elastic medium (from Misra, 2010).	9
2.2	Point and distributed forces acting on the needle during insertion (from Roesthuis, 2012).	10
2.3	Nonholonomic model in which the needle tip is represented as a bicycle with a fixed front-wheel steering angle (from Webster, 2006).	11
2.4	Mechanical model of a needle in a two-bend configuration (from Roesthuis, 2012).	13
2.5	Custom-manufactured steerable needle with an actuated tip and integrated Fiber Bragg Grating strain gauges (from Roesthuis, 2015).	15
2.6	Example of a steerable concentric-tube needle with three segments (from Rucker, 2010).	16
2.7	Alternating-planes strategy to track the needle tip during insertion (from Patel, 2015).	17
2.8	Needle tracking in US via imaging in the transverse plane (from Vrooijink, 2014).	19
2.9	Catheters semi-automatically segmented in 3D MRI data using the NeedleFinder Slicer extension (from Pernelle, 2013).	20
2.10	Placement of Fiber Bragg Grating sensors on a specially-modified needle (from Roesthuis, 2014).	21
3.1	Given a number of samples, the spacing between the samples d , the offset distance from the needle tip δ , and a new needle base pose, the expected coordinate of the needle p_k is calculated at each sample point.	32
3.2	New imaging is collected at each needle coordinate, and the actual position of the needle is observed.	33

3.3	A new polynomial curve is calculated, optimized to minimize both the cumulative bending energy in the needle and the error between the curve and the observed points.	34
4.1	System architecture for needle detection and modeling from MRI data.	37
4.2	User interface for MRINeedleTipTracker 3D Slicer module.	37
4.3	Example tissue phantom with the needle alignment frame and biopsy needle.	39
4.4	Segmentation of needle artifact generated by thresholding MRI volume.	40
4.5	Baseline ground truth data, calculated from the centroids of the segmented artifact sectioned in the X-Y plane.	41
4.6	Magnitude of in-plane error over insertion for various degrees of polynomial. Markers indicate the positions of the slices on the needle curve. $d = 26.0mm, k = 3, \delta = 5.0mm$	42
4.7	Magnitude of in-plane error over insertion for a variable number of sample points. Markers indicate slice positions. $n = 5, \delta = 5.0mm$	43
4.8	Positions of 2D scan planes at each insertion step, with segmented artifact.	44
4.9	Modeled curve points at each insertion step, with segmented artifact.	45
4.10	Magnitude of error between the needle model and the artifact centroid with fixed spacing between slices. Markers indicate slice positions. $d = 10mm, k = 3, \delta = 5mm$	46
4.11	Magnitude of error between the needle model and the artifact centroid, where the spacing between each slice increases with insertion depth. Markers indicate slice positions. $d = 10mm + index_{step} * 4mm, k = 3, \delta = 5mm$	47

Chapter 1

Introduction

1.1 Motivation

Many interventional procedures rely on needle insertion, including biopsy and brachytherapy [1]. Accurate needle placement is a critical factor in the success of these procedures [2, 3]. Deflection of the needle tip during insertion and variation in the mechanical properties of tissue can cause the needle to deviate from its expected trajectory and miss the target. This can be mitigated by aligning the needle to the target using a fixed structure and verifying that the correct position has been reached in post-operative imaging [4]. Even with preoperative image-based planning and careful alignment with the target, several insertions may be required to achieve the desired needle placement [5].

Live intra-operative imaging of the needle during insertion reduces error caused

by needle deflection by allowing the surgeon to see if the needle is deviating from its trajectory and take corrective action. Ultrasound (US) and Magnetic Resonance Imaging (MRI) are preferred imaging modalities. While US is portable and hand-steerable, MRI offers superior resolution of soft tissues compared to both US and CT [6]. Even with intraoperative imaging, manually-controlled needle insertion is a challenging task. As shown in Figure 1.1, the confined space of the MRI scanner bore limits the surgeon's visibility and range of motion [7].

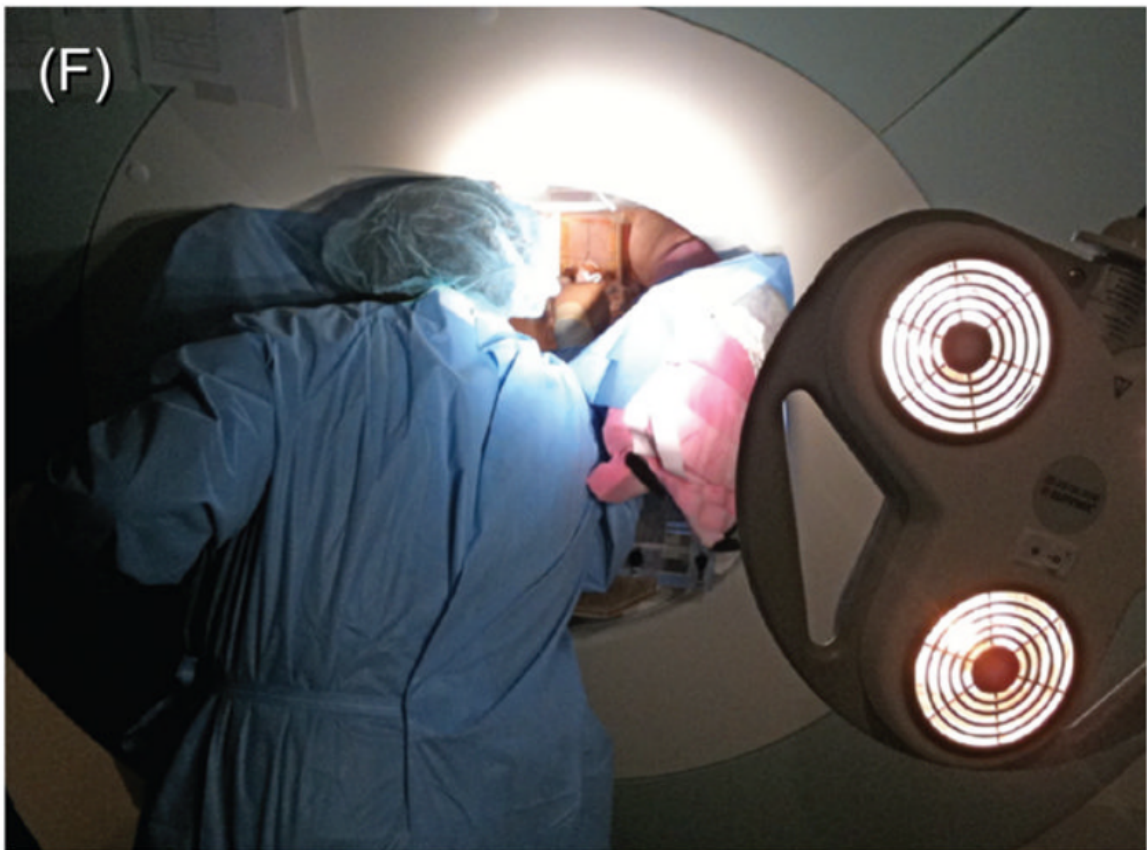


Figure 1.1: A manual MRI-guided biopsy in progress (from Tokuda, 2012).

Robotically-controlled needle insertion solves some of the challenges of live intra-

operative MRI imaging by reducing the clinician’s workload and moving them out of the scanner bore. Using live imaging, an insertion robot can correct for unmodeled tip deflection and keep the needle on its expected trajectory, improving the accuracy of needle placement.

Previous work has shown that closed-loop control of MRI [8] and US [9] coupled with image analysis for needle localization can track the needle tip during insertion with a useful degree of accuracy.

1.2 Problem Formulation

A key requirement for closed-loop image-guided needle insertion is the accurate measurement of the 6-degree-of-freedom pose of the needle tip using data from the imaging system. Accurate tip localization is required for the needle controller to determine the correct control input to minimize the error between the current needle tip pose and the desired trajectory. Searching for the needle in each image on an individual basis introduces errors due to imaging artifacts, noise, and anatomical features near the needle, contributing to reduced tip localization accuracy. A needle model that could combine data from real-time imaging, from the robotic insertion platform, and the mechanical properties of the needle would allow accurate estimation of the pose of the needle tip from sparse observations of the needle position.

1.3 Thesis Contributions

1.3.1 Minimum Bending Energy Model

This thesis presents an approach to needle modeling that uses the mechanical bending properties of the needle, the pose of the needle base, and a set of observed needle positions along the needle shaft to find a configuration of the needle that minimizes its bending energy while meeting the observed constraints. In this model the needle is represented by a three-dimensional parametric polynomial curve.

1.3.2 Needle Localization Algorithm

The needle model provides continuous needle pose estimates along its shaft, which can be used to plan imaging to observe the needle position after motion. The expected position of the needle informs the search for the actual position of the needle in received images, which reduces localization error caused by noise near the needle. Since the needle model is updated using a set of positions along the needle shaft instead of the position of the needle tip, updates can be performed using imaging in planes transverse to the needle rather than imaging in the coronal and sagittal planes. This mitigates the risk of loss of needle tracking during insertion.

1.3.3 MRI Data Collection

MRI scans were collected depicting the insertion of a biopsy needle into a gelatin tissue phantom. An alignment structure restricted the pose of the needle base during insertion, allowing scans taken at regular insertion interval to be associated with needle poses.

1.3.4 Slicer Module

An extension for 3D Slicer, an open-source medical imaging program [10, 11], was created to evaluate the needle model when applied to the MRI dataset. The user interacts with the needle model through the Needle Tracking module, which accepts inputs for the current needle base pose and the current 3D scan in the MRI dataset and returns polynomial coefficients representing the current state of the needle. A supporting MRI Reslicer module converts the 3D MRI scans into 2D slices at specified depths, which simulates part of the functionality of an MRI machine.

1.4 MRI Physics

Magnetic Resonance Imaging (MRI) is used to image material containing hydrogen ions, or protons, such as human tissue. The strong magnetic field of the MRI machine causes the free protons to align along the axis of the field. A pulse of radiofrequency (RF) radiation excites the protons, which subsequently emit RF energy as they return

to a lower-energy state. The emitted energy is measured by the scanner to generate and image of the tissue based on the intensity of the return from different areas.

Performing an MRI scan on a material that does not contain any free protons, such as plastic or metal, produces a dark void in the image [12]. Metal objects distort the magnetic field, producing susceptibility artifacts around the objects. The shape and extent of each artifact depends on the parameters of the MRI scan sequence the the shape and composition of the object. Needles and wires behave like antennae in the MRI environment, so they produce imaging artifacts around their tips. Determining the position of the needle using its imaging artifact is the basis for needle tracking in MRI [13].

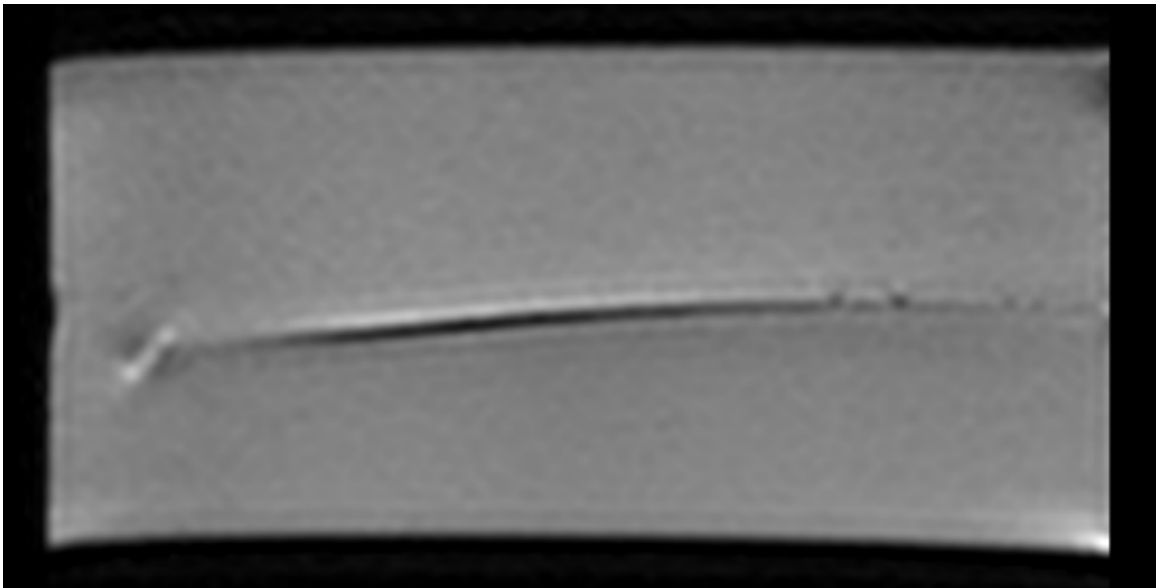


Figure 1.2: MRI scan of a gelatin tissue phantom undergoing needle insertion. The needle enters the phantom at the right of the image. Note the artifact around the needle tip.

1.5 Tissue Phantoms

Synthetic tissue phantoms are often used during needle insertion studies instead of ex-vivo tissue specimens. These phantoms are manufactured so their mechanical properties reflect those of human tissue. They offer several benefits over real tissue, especially in the context of benchtop laboratory experiments.

1. Phantoms made of gelatin or plastic are transparent, so vision-based methods can be used for needle tracking or for validation of other imaging modalities.
2. A needle inserted into a homogeneous tissue phantom will experience constant cutting force throughout insertion.
3. Phantoms can include multiple regions with different mechanical properties separated by membranes.
4. Phantoms have a much longer shelf life than tissue, granting more flexibility to studies.

Chapter 2

Review of Previous Work

2.1 Needle Geometry

Beveled-tip needles deflect during insertion due to asymmetric cutting force at the needle tip. The tip force, shown in Figure 2.1, can be modeled as a point load with transverse and radial components relative to the needle shaft [14]. Friction and fluid damping are transverse forces distributed along the needle shaft, while pushback from deformed tissue is a distributed radial force. Figure 2.2 shows the point and distributed loads on the needle shaft.

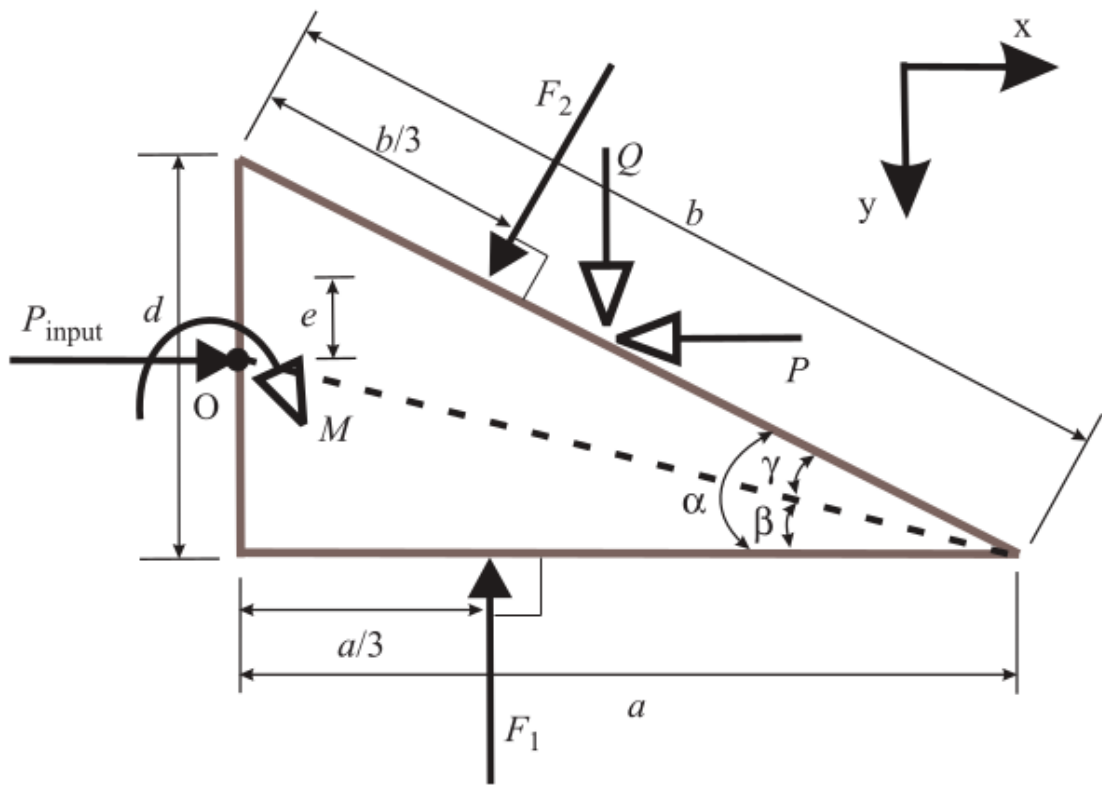


Figure 2.1: Free-body diagram depicting forces acting on an asymmetric beveled needle tip during insertion into an elastic medium (from Misra, 2010).

2.2 Needle Modeling

The goal of research in this area is to produce a model of needle behavior that accurately predicts the motion of the needle tip during insertion. If the model accurately represents the behavior of the needle, a trajectory can be planned and accurately followed even when few or no needle tip observations can be made.

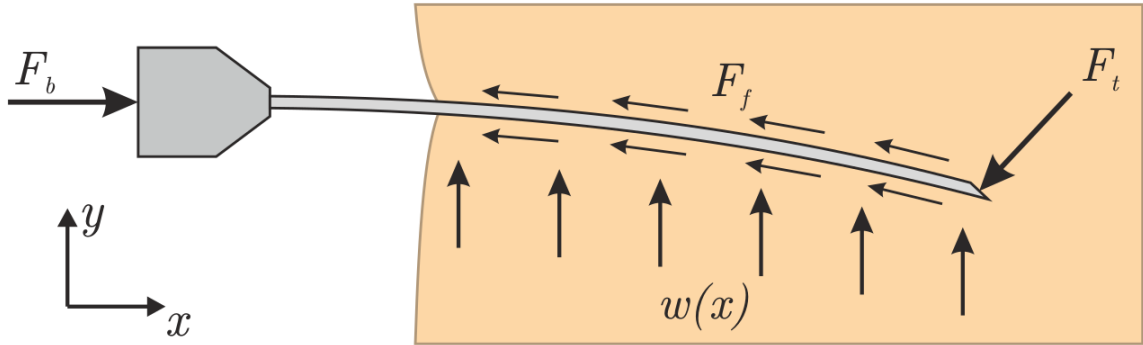


Figure 2.2: Point and distributed forces acting on the needle during insertion (from Roesthuis, 2012).

2.2.1 Non-Holonomic Kinematics

The non-holonomic kinematics of a beveled-tip needle can be represented by modeling the needle as a bicycle with the front wheel fixed at a constant steering angle [15, 16]. This model is illustrated in Figure 2.3. Since the steering angle is determined by the shape of the needle, the stiffness of the tissue, and the velocity of insertion, steering angles must be calculated for individual insertions.

Subsequent work accounts for forces on the needle that cannot be modeled as components of the steering angle, such as dynamic friction and torsion in the needle shaft [17, 18]. These improved models still assume a constant steering angle, which implies that the needle is inserted into a homogeneous material. This assumption does not apply for most insertions into tissue, limiting the utility of the nonholonomic kinematic model for clinical applications.

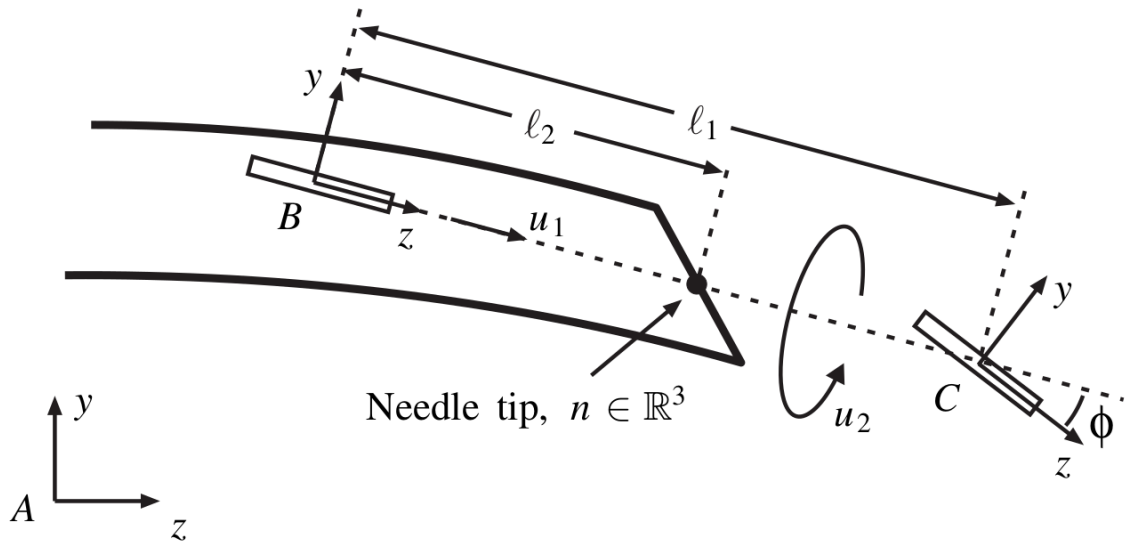


Figure 2.3: Nonholonomic model in which the needle tip is represented as a bicycle with a fixed front-wheel steering angle (from Webster, 2006).

2.2.2 Finite Element Models

Finite Element (FE) models of the needle and surrounding medium address some of the drawbacks of the kinematic needle model, such as the ability to model inconsistent deflection when inserting through nonhomogeneous tissue [19]. FE model-based approaches use several types of finite elements, including angular springs and beam elements. While the needle and environment are often simplified as a 2D mesh in a plane, the approach is extensible to 3D [20].

FE modeling requires an explicit definition of the sliding interface between the needle shaft and the surrounding tissue and representation of the elastic mechanical properties that govern the deformation of tissue during insertion [21]. Since the needle is slender and the magnitude of deflection is large relative to the needle diameter,

the assumption of linear displacement usually applied to FE analysis does not hold and a computationally-intensive numerical solver is required to solve for nonlinear displacement.

2.2.3 Mechanical Models

The needle can also be modeled as an Euler-Bernoulli beam, with the forces acting on the needle divided into a force acting on the needle tip and a distributed load acting on the needle shaft. The tip force is related to the force required to cut through the tissue, which depends on the insertion velocity [22]. The distributed shaft load depends on the stiffness and viscous coefficient of the tissue [23].

Another approach is to represent the shape of the needle as a polynomial and use mechanical bending energy to choose the polynomial coefficients [14, 23, 24]. This accounts for needle deflection and deformation of surrounding tissue, which allows calculation of the force on the needle base.

Mechanical models require explicit definitions for the elastic modulus, stiffness, and cutting force of the tissue and the elastic modulus of the needle. These properties might be unknown during a clinical insertion, and it might not be possible to measure them experimentally. The tissue is generally assumed to be homogeneous, which is not always applicable.

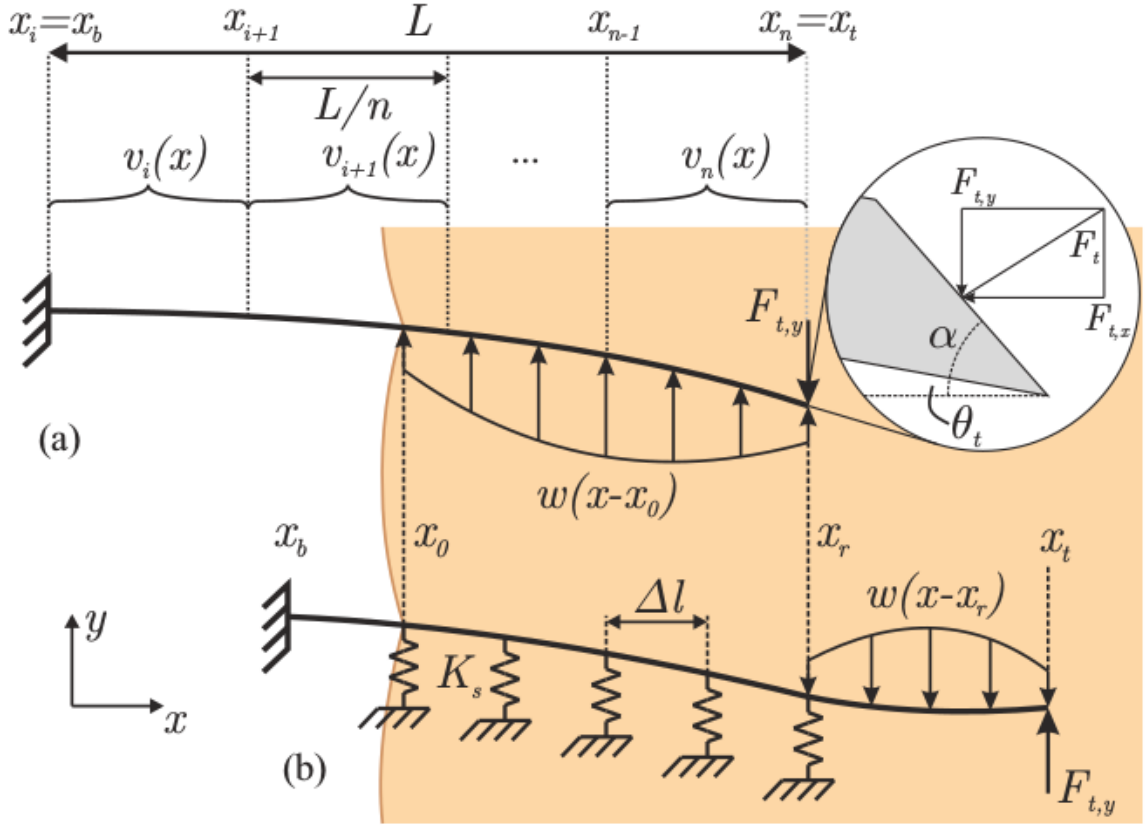


Figure 2.4: Mechanical model of a needle in a two-bend configuration (from Roesthuis, 2012).

2.3 Needle Steering

The different approaches to needle steering can be generalized as minimally-invasive methods to guide a needle to a desired point in the body using control inputs applied from outside the body. The various methods produced in this line of research can be placed along a spectrum of mechanical complexity in the needle shaft and at the needle tip, ranging from solid needles controlled only at the base, to needles with actuation at the tip and along the shaft, to continuum robots.

Most needle steering strategies rely on the asymmetric force at the tip of a beveled

needle as a control input to direct the needle along a desired trajectory. Rotating the needle tip changes the direction of the force vector acting on the tip, allowing the direction of deflection to be controlled. Steering algorithms that take advantage of this behavior include duty cycle steering [25], CURV steering, and continuous-rotation steering.

Symmetric-tip needles are not subject to significant asymmetric tip force during insertion [26]. While the magnitude of deflection during insertion is reduced, the direction of deflection is inconsistent, so symmetric-tipped needles cannot be steered by rotating the needle tip. An alternative strategy steers the needle by moving its base outside the tissue, which induces a bend in the needle shaft [27].

Curved- or kinked-tip needles use similar mechanical principles to steer as beveled-tip needles, but the addition of a pre-bent section at the needle tip greatly increases the asymmetric force applied to the needle tip during insertion [28]. This allows the needle to achieve a tighter turning radius, especially if the needle shaft is thin and made of a very flexible material such as nitinol. Kinked-tip needles cause more tissue damage than beveled-tip needles when steered using a rotation-based strategy, but needles with passively-actuated tips have been developed to mitigate this by straightening during continuous rotation [29]. Needles with fully-actuated tips can be steered along a trajectory without rotating the needle [24]. A disadvantage of curved-tip needles is that the tip translates during rotation, which violates the nonholonomic kinematic model's assumption that the needle will only move along the tip vector [28].

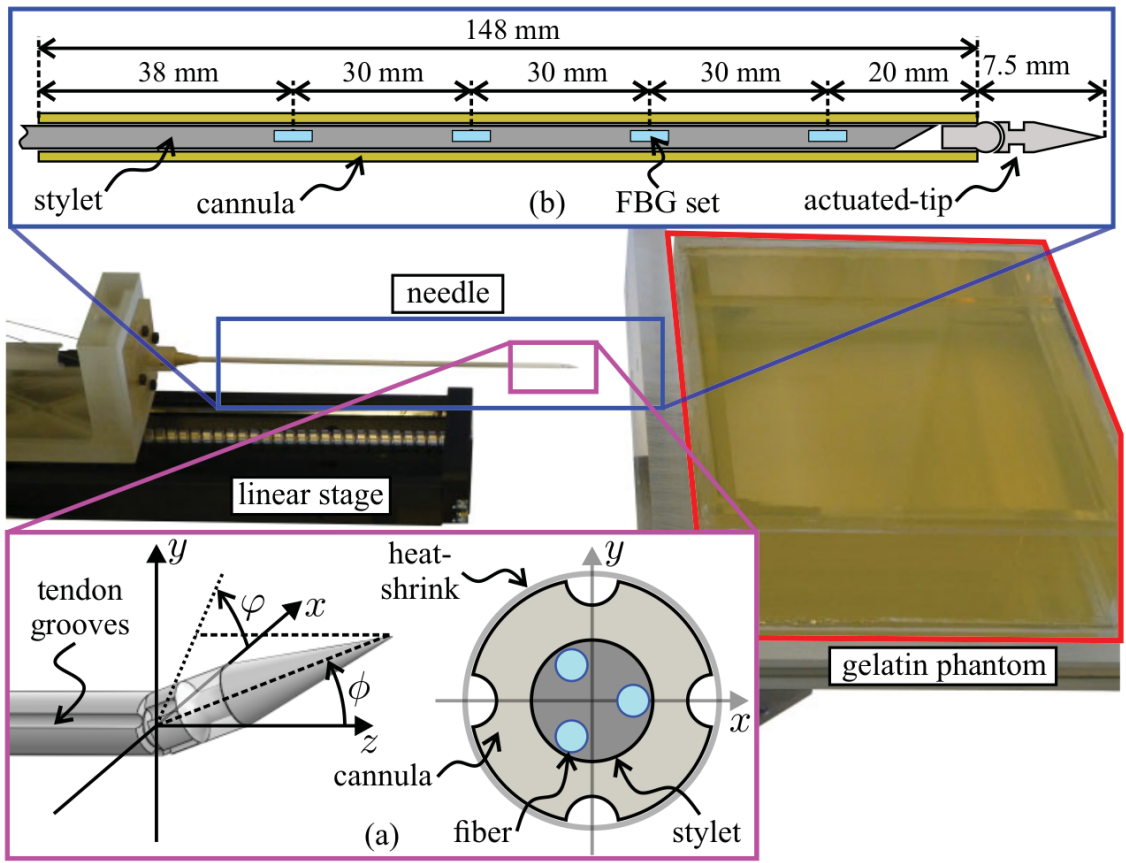


Figure 2.5: Custom-manufactured steerable needle with an actuated tip and integrated Fiber Bragg Grating strain gauges (from Roesthuis, 2015).

Concentric-tube needles consist of several nested pre-bent tubes [30–32]. An example with three concentric segments is shown in Figure 2.6. The needle can be actively curved or straightened by rotating the tubes so their directions of curvature are aligned or in opposition. These needles release energy when the concentric elements snap between equilibrium states, which may be undesirable.

A problem with approaches based around specialized needles is that no clinically-available biopsy needles of these types exist. With specialized needles there is an increased risk of tissue damage along the insertion trajectory, especially if the needle

is rotated.



Figure 2.6: Example of a steerable concentric-tube needle with three segments (from Rucker, 2010).

2.4 Needle Localization

Existing needle localization algorithms generally analyze individual scans or video frames in isolation. It would be very useful to use the results from processing a previous image to find the needle in the current image. The forward kinematics of the insertion platform, especially the change between the current state and a previous state, could also be used to find the new needle position in new images.

2.4.1 Coronal and Sagittal Plane Imaging

Prior work by our research group demonstrated needle tip tracking using closed-loop MR imaging in the coronal and sagittal planes [8]. As shown in Figure 2.7, the needle tip is captured in each scan plane and the coordinate of the centroid of the tip artifact is used to plan the pose of the subsequent scan in the perpendicular plane. The field of view of each plane is sized based on the maximum anticipated deflection of the needle between scans.

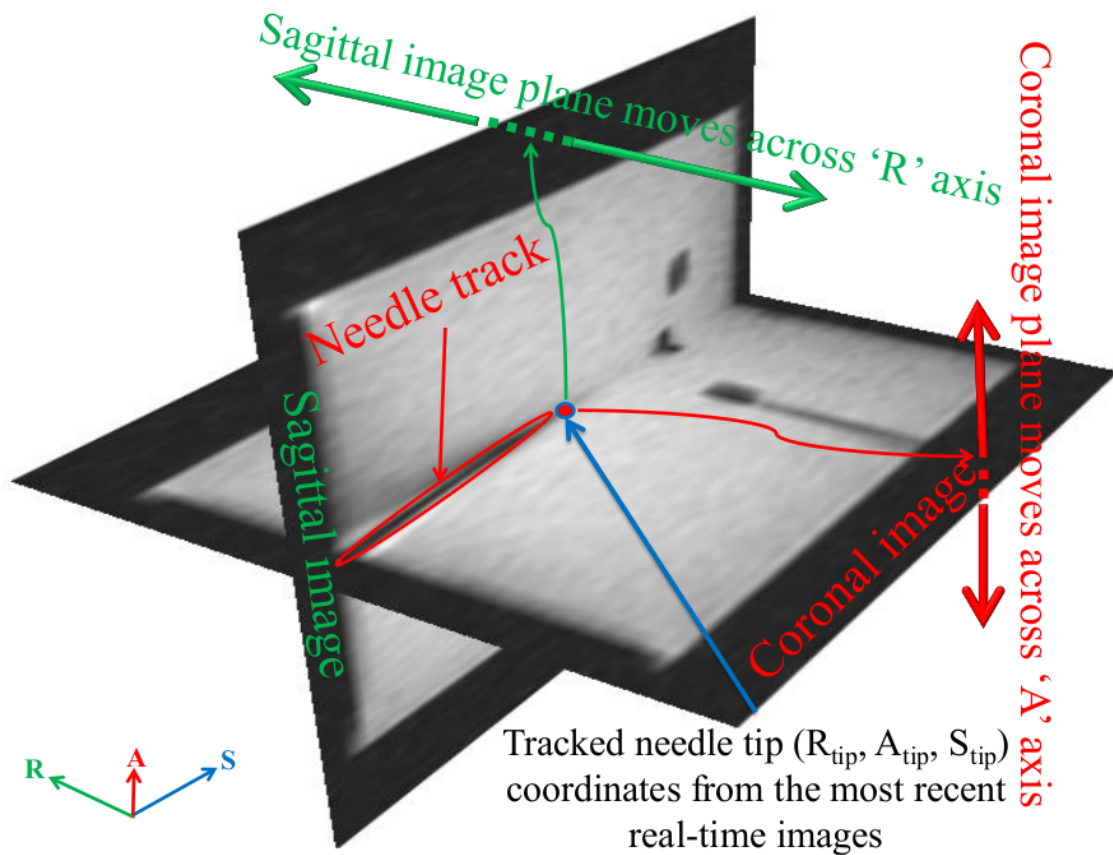


Figure 2.7: Alternating-planes strategy to track the needle tip during insertion (from Patel, 2015).

A major risk with this approach is the loss of tracking if the needle tip is not found in one of the scans. The key piece of information used to plan the position of each scan is the location of the needle tip in the immediately-previous scan. Since the scan planes are parallel to the needle shaft and might be a few millimeters thick, a small error in the placement of one scan plane could result in failure to capture the needle. This risk can be mitigated by specifying a scan plane thickness sufficient to capture the needle tip even if it deflects significantly between scans. However, thick scan planes reduce the clarity of features in MR images, which would be detrimental for identifying anatomical features near the needle.

2.4.2 Transverse Plane Imaging

Imaging in the plane normal to the needle shaft captures the needle in cross-section. This reduces the risk of taking a scan in a plane that does not contain the needle, but because of tip deflection it is more challenging to find the plane containing the needle tip. For US scanning [9,33,34], the transducer can be mounted on a motorized platform and moved in synchronization with the calculated out-of-plane motion of the needle tip to capture the same point on the needle in cross-section throughout insertion, as shown in Figure 2.8.

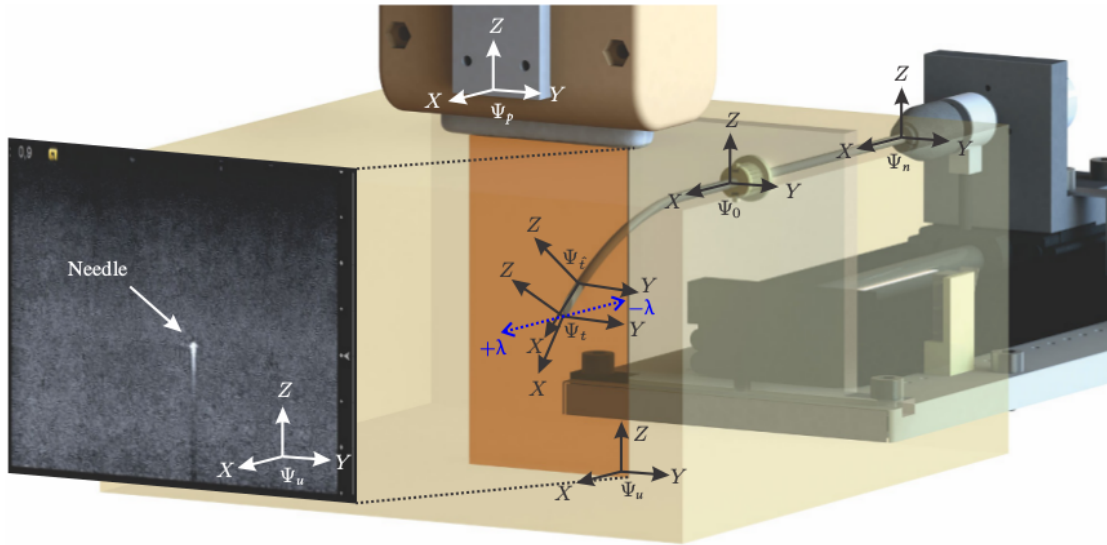


Figure 2.8: Needle tracking in US via imaging in the transverse plane (from Vrooijink, 2014).

2.4.3 3D Imaging

NeedleFinder is a 3D Slicer extension for needle localization and segmentation [35]. Given a manually-selected tip position, NeedleFinder searches through sequential axial scan planes and finds the cross-sections of the artifacts or voids in each layer. An angular-spring finite element model defined by the shape and stiffness of the needle is fit to the detected needle points. Figure 2.9 shows several catheters segmented using NeedleFinder. Manual selection of each needle tip is required because of the difficulty of automatically distinguishing each needle from anatomical features and noise in the MR images.

Other research models susceptibility artifact shapes for metal fiducial markers in MR data to automatically segment the markers and determine their poses [36]. This

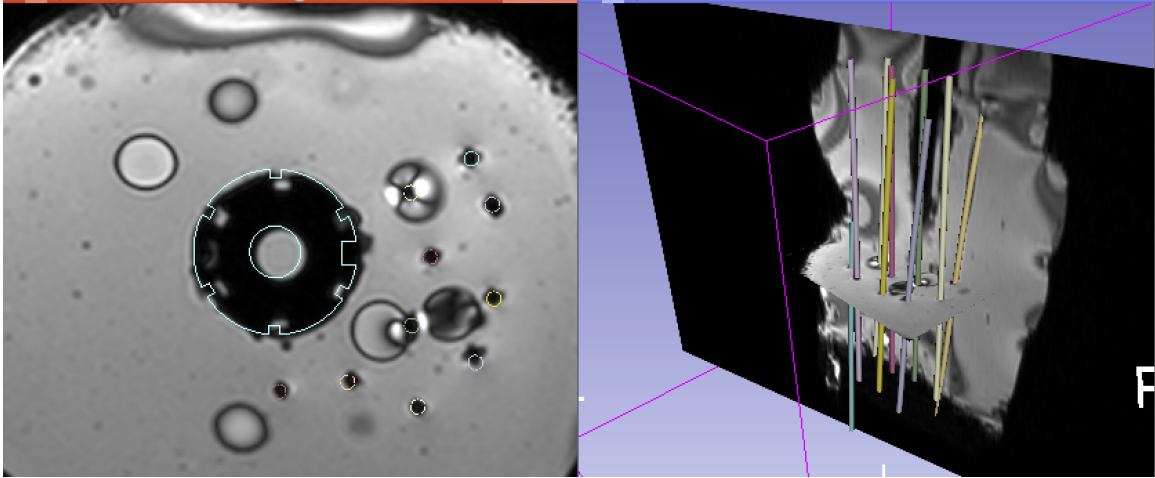


Figure 2.9: Catheters semi-automatically segmented in 3D MRI data using the NeedleFinder Slicer extension (from Pernelle, 2013).

approach could probably be extended to detect needle tip poses from tip artifacts with greater precision than thresholding by intensity, but the variation in the needle artifact with the orientation of the needle relative to the direction of the magnetic field would require experiments to characterize it in detail.

In both US and MR images, the time required to resolve a 3D volume is higher than for a 2D plane, so 3D imaging is generally not suitable for real-time tracking or control.

2.4.4 Other Techniques

An alternative method for detecting the position and shape of the needle is to add sensors to the needle to directly measure its deflection. One approach, shown in Figure 2.10 is to embed Fiber Bragg Grating optical sensors into the shaft of the

needle [37]. These sensors measure the strain in the needle as it bends and allow the shape of the needle to be calculated throughout insertion to achieve robotic steering. This approach requires specially-modified needles, precluding the use of clinical-style biopsy needles without modification.

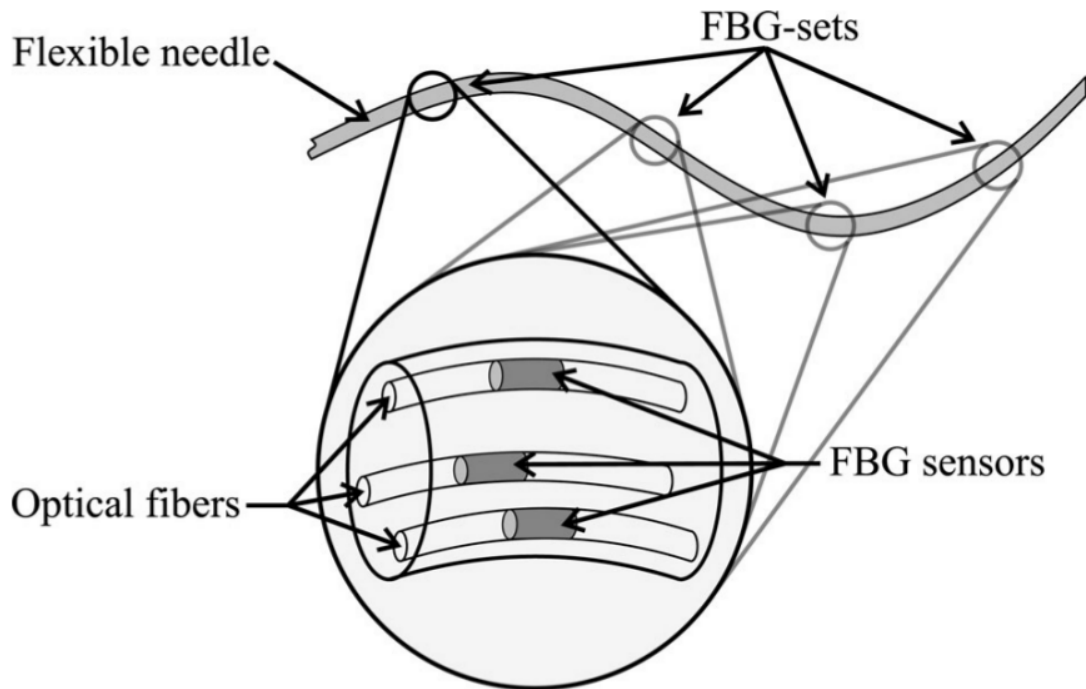


Figure 2.10: Placement of Fiber Bragg Grating sensors on a specially-modified needle (from Roesthuis, 2014).

Another option is to attach magnetic tracking coils to the needle shaft and use an external sensor unit to measure their 6-DOF poses and compute the needle shape [38, 39]. As the magnetic tracking sensor uses a sensitive magnetic field to measure the poses of the fiducial markers, this is not compatible with the strong magnetic field produced in the MRI environment.

Chapter 3

Needle Model

The needle model presented in this thesis is based on minimizing the bending energy in the needle, which is represented as a beam and characterized as a parametric polynomial curve. The model is initialized with the mechanical properties of the needle and updated throughout insertion with the most recent needle base pose and the latest observed points on the needle shaft. This allows estimation of the shape of the needle using only a few new images without requiring an explicit model of the forces acting on the needle.

While other approaches to needle modeling account for bending energy, generally to determine the equilibrium state between the needle and the surrounding elastically-deformed tissue [14, 23, 24], they do not use bending energy to find the shape of the needle from observations.

Mechanics-based models make restrictive assumptions about the trajectory of the

needle by limiting the number bends in the needle shaft [23]. Models that assume a single direction of insertion [23, 40] cannot represent the trajectories achievable with highly-flexible needles. By parameterizing the needle coordinates independently of the insertion direction or depth, the model presented here can represent needles inserted in any direction relative to the scanner coordinate frame.

Both nonholonomic kinematic models [15,17,18] and mechanics-based beam bending models [23, 40] require extensive characterization of the properties of the needle and the tissue in order to accurately account for the tip and shaft loads placed on the needle. Tissue properties vary between tissue types and patients, and characterization of these properties to the extent required by the needle models would probably not be practically achievable during a procedure. In contrast, the model introduced here does not require characterization of mechanical properties, since the constraints imposed on the needle by its interaction with surrounding tissue are observed through the shape of the needle during insertion.

In the context of needle localization in MRI, it would be very time-consuming to completely and precisely evaluate the state of the needle using only observations from imaging. The core idea of this model is to take a few observations in imaging and then determine the shape of the needle through optimization that meets those constraints as well as the constraints imposed by the mechanics of the needle. Provided that the observations of the needle are distributed along the entire observable portion of its length, the needle model will be representative of the actual state of the needle to a

degree of accuracy useable for guiding insertion and planning future imagery.

3.1 Assumptions and Definitions

As currently formulated, this model only considers straight needles with uniform stiffness and cross-section. Actuated devices such as flexible-tip needles and continuum robots are not considered. It is also assumed that the state of the needle relative to the camera frame is observable in imaging.

The model uses the following information about the composition and state of the needle:

- 6-degree-of-freedom pose of the base of the needle, via the forward kinematics of the insertion robot
- Length of the needle
- Diameter of the needle
- Elastic modulus of the needle
- Multiple observed coordinates on the needle shaft from a sparse set of cross-sectional images

Definitions of the symbols used in the needle model are provided below.

Symbol	Description
C	cumulative cost of the needle model configuration
d	needle shaft diameter
δ	needle tip offset
E	needle shaft elastic modulus
ϵ	needle curve RMSE threshold
I	second area moment of inertia
k	observation index
L	needle length
n	polynomial degree
ρ	needle curvature
s	parametric variable
U_B	transverse beam bending energy
v	magnitude of deflection relative to the needle neutral axis
\mathbf{V}	vector, needle coordinate
\mathbf{V}_{obs}	vector, needle coordinate observed in imaging
$x \in X$	X-component , set of X-components of needle coordinate
$y \in Y$	Y-component , set of Y-components of needle coordinate
$z \in Z$	Z-component , set of Z-components of needle coordinate

3.2 Beam Bending Energy

The actual biopsy needle contains several components with different mechanical properties, such as an inner rod that slides within an outer shell. Since these interactions are computationally expensive to model exactly and unnecessary to account for unless a very high degree of fidelity is desired, the model presented here simplifies the needle as a solid cylindrical beam and neglects the change in cross-sectional area at the needle tip. Under these assumptions, the area moment of inertia I of the needle in cross-section is constant along the entire length of the needle, so the area moment of inertia can be calculated using Equation 3.1.

$$I = \frac{\pi}{64}d^4 \quad (3.1)$$

Since the needle is assumed to have a constant diameter d along its entire length, it can be represented as an Euler-Bernoulli beam with constant cross-sectional area. The transverse bending energy in a straight beam with constant cross-section, shown in Equation 3.2, is a function of the curvature in the beam integrated over its length. Equation 3.3 shows the calculation of curvature in an arc. If the first derivative of the needle deflection dv/dl is very small, the curvature can be approximated as Equation 3.4.

$$U_B = \frac{EI}{2} \int_0^L \frac{1}{\rho^2} dl \quad (3.2)$$

$$\frac{1}{\rho} = \frac{d^2v/dl^2}{(1 + (dv/dl)^2)^{3/2}} \quad (3.3)$$

$$\frac{1}{\rho} \simeq \frac{d^2v}{dl^2} \quad (3.4)$$

In a beam subject to zero load its cumulative curvature is zero, so its total bending energy is also zero. Higher curvatures correspond to sharper bends, meaning that a beam that is predominately straight with one very sharp bend will have a greater bending energy than a beam of the same length where the bend is gentle and distributed along its entire length. Beams adopt shapes that minimize their cumulative bending energy while meeting the constraints imposed by external fixtures.

3.3 Parametric Polynomial Space Curves

The needle curve is represented using an n -degree parametric polynomial function, shown in Equation 3.5. In the context of representing a needle, n represents the maximum number of inflection points in each axis. Under ideal conditions a needle inserted without rotation would deflect in one direction with constant curvature, and its shape could be represented using at minimum a 3rd-degree polynomial ($n = 3$).

$$\mathbf{V} = \begin{bmatrix} x(s) \\ y(s) \\ z(s) \end{bmatrix} = \begin{bmatrix} a_n s^n + a_{n-1} s^{n-1} + \dots + a_1 s + a_0 \\ b_n s^n + b_{n-1} s^{n-1} + \dots + b_1 s + b_0 \\ c_n s^n + c_{n-1} s^{n-1} + \dots + c_1 s + c_0 \end{bmatrix} \quad s \in (0, 1) \quad (3.5)$$

The three spatial coordinates x , y , and z are functions of a unitless parameter s , which ranges from 0 at the needle base to 1 at the needle tip. Given sets of k needle coordinates \mathbf{V}_{obs} , the relationship between the values of s and the positions of the needle coordinates is established by the distances between the needle coordinates, calculated in Equation 3.6, and the proportion of each distance to the cumulative distance between all the coordinates, calculated in Equation 3.7.

$$\begin{cases} d_k = 0 & \text{if } k = 0 \\ d_k = |\mathbf{V}_{obs,k} - \mathbf{V}_{obs,k-1}| & \text{if } k > 0 \end{cases} \quad (3.6)$$

$$\begin{cases} s_k = 0 & \text{if } k = 0 \\ s_k = s_{k-1} + \frac{d_k}{L_{needle}} & \text{if } k > 0 \end{cases} \quad (3.7)$$

While an alternative implementation could represent the x - and y -components of the coordinate as a function of its z -component, representing all three coordinates as functions of an independent parameter allows the curve to represent torturous trajectories without placing restrictions on the direction of needle insertion.

The maximum number of inflection points in each axis, and consequently the

maximum number of changes in needle direction that the curve can represent, is limited by the degree of the polynomial.

3.4 Curve Fitting

The purpose of curve fitting is to choose coefficients of the parametric function in Equation 3.5 given a number of observed needle cross section coordinates so that the total bending energy in the curve and the error between the curve and the needle coordinates are minimized.

Prior to optimization, initial coefficients for each curve are found by fitting a polynomial of degree n to the needle coordinates using a least-squares fit. While this initial solution is not representative of the actual mechanical factors that determine the shape of the needle, it approximates the minimum bending energy curve and helps prevent the optimization for reaching a local minimum or other failure condition.

The curve is optimized to minimize bending energy using Sequential Least Squares Programming (SLSQP), which is an iterative constrained Non-Linear Programming (NLP) search algorithm [41].

3.4.1 Cost Function

The cost function subject to minimization is shown in Equation 3.8. It is a modification of Equation 3.2 where the elastic modulus and area moment of inertia

are omitted, since they are constant along the length of a straight needle with uniform cross-section.

$$C = \int_0^L \frac{1}{\rho^2} dl \quad (3.8)$$

3.4.2 Constraints

The optimization is constrained by Equation 3.9 such that the coordinates of the curve at $s = 0$ matches the position of the base of the needle.

$$\mathbf{V}_{k=0} = \begin{bmatrix} a_0 \\ b_0 \\ c_0 \end{bmatrix} \quad (3.9)$$

The optimization is further constrained by Equation 3.10 so that the length of the curve between $s = 0$ and $s = 1$ is equal to the length of the needle, and by Equation 3.11 so that the root-mean-square error (RMSE) between the curve and the observed points is below a specified threshold ϵ .

$$L = \int_0^1 \left| \frac{d\mathbf{V}}{ds} \right| ds \quad (3.10)$$

$$\epsilon \geq \sqrt{\frac{\sum_{i=0}^k (V_i - V_{obs,i})^2}{k}} \quad (3.11)$$

While equality constraints can also be used to guide the optimized curve to intersect all the needle coordinates, this approach risks over-constraining the curve where the degree of the polynomial is close to the number of equality constraints.

3.5 Software Implementation

Algorithm 1 shows the process of calculating polynomial coefficient to minimize bending energy given a set of observed needle coordinates. Figures 3.1, 3.2, and 3.3 show the process of observing points near the modeled needle curve and optimizing a new curve to match them.

Algorithm 1 Curve Optimization

```

1: procedure UPDATE CURVE FIT( $coords_{needle}, L_{needle}, poly_{prev}$ )
2:    $t \leftarrow CalculateParameters(coords_{needle}, L_{needle})$ 
3:   if  $poly_{prev}$  is None then
4:      $poly_{init} \leftarrow LeastSquares(coords_{needle})$ 
5:   else
6:      $poly_{init} \leftarrow poly_{prev}$ 
7:    $cons \leftarrow DefineConstraints(t, coords_{needle}, L_{needle})$ 
8:    $poly_{opt} \leftarrow DoOptimization(poly_{init}, cons)$ 
9:   return  $poly_{opt}$ 

```

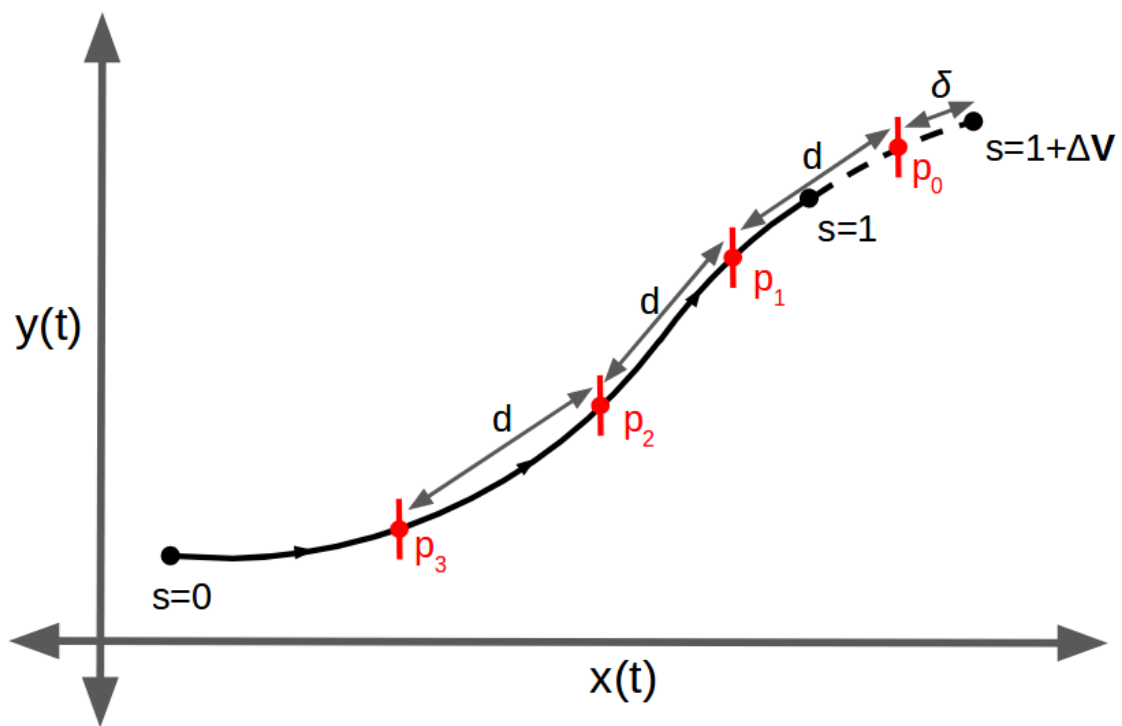


Figure 3.1: Given a number of samples, the spacing between the samples d , the offset distance from the needle tip δ , and a new needle base pose, the expected coordinate of the needle p_k is calculated at each sample point.

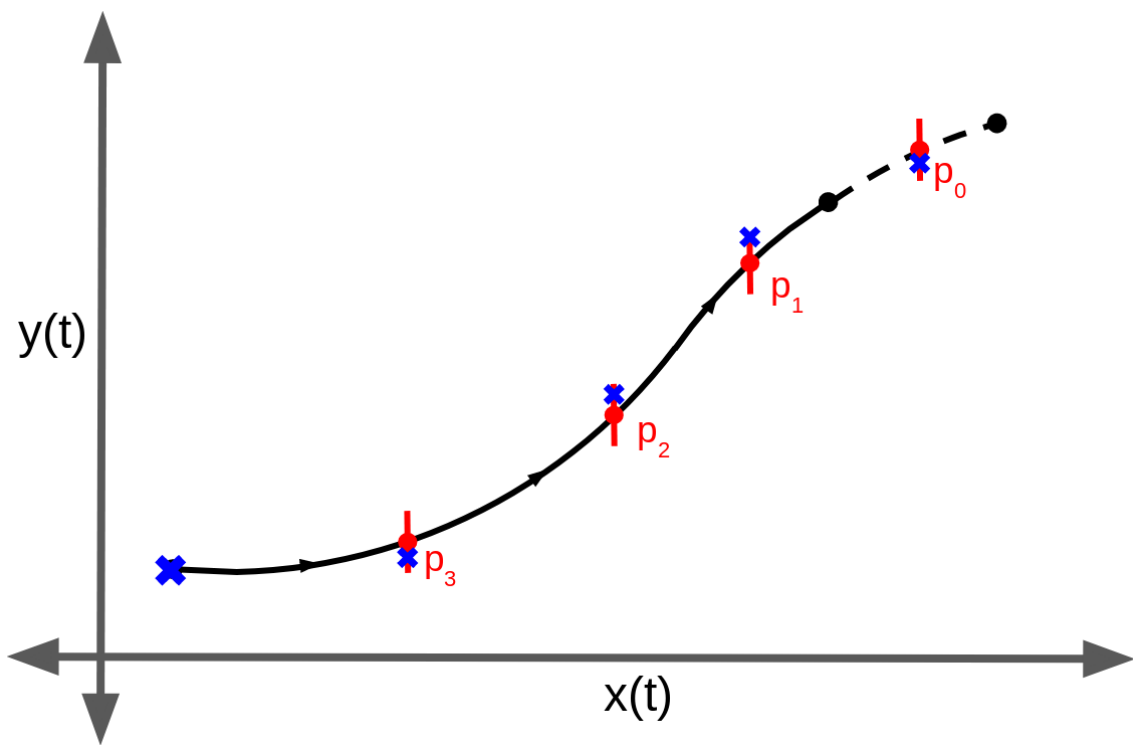


Figure 3.2: New imaging is collected at each needle coordinate, and the actual position of the needle is observed.

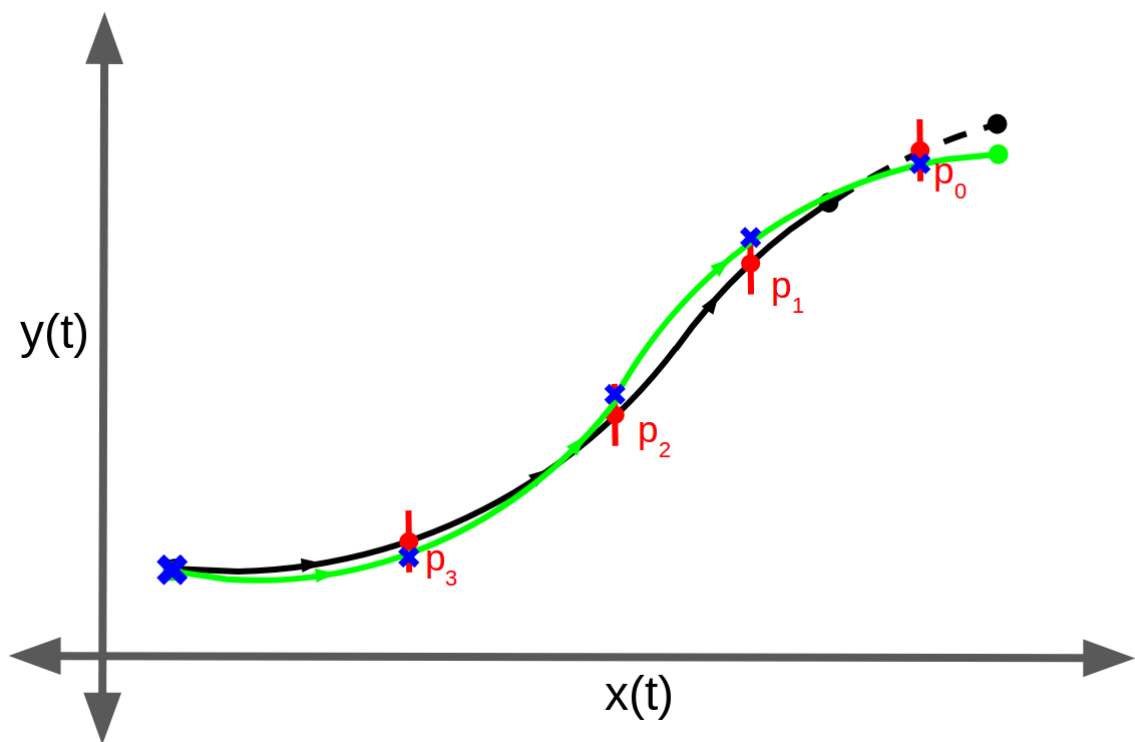


Figure 3.3: A new polynomial curve is calculated, optimized to minimize both the cumulative bending energy in the needle and the error between the curve and the observed points.

Chapter 4

Needle Localization in MR Images

The purpose of this experiment is to validate the needle model on imagery representative of what would be available from intraoperative imagery during an MRI-guided insertion and to demonstrate a workflow suitable for real-time needle tracking.

4.1 Software Architecture

4.1.1 Simulated MRI Scanner

Full 3D MRI volumes take a long time to produce, especially if high resolution is desired: the scan time for each volume used in this thesis was approximately 5 minutes. This is a prohibitively long time in the context of real-time intraoperative imaging, so the MRI would be configured to provide 2D scans in requested planes with limited field of view. To simulate this functionality, a Slicer module was created

to resection 2D slices from each 3D volumes at specified depths.

4.1.2 Needle Tracking Module

A second Slicer module manages the needle tracking process. Figure 4.1 shows the architecture of this module relative to the Slicer environment and the needle modeling utility. A linear transform node is set to match the pose of the needle base in each saved volume. When commanded by the operator, the module requests slices of the MRI volume at evenly-spaced coordinates along the shaft of the needle. The thresholded image is grouped into contiguous regions, and the area and centroid are calculated for each region. The region with the centroid closest to the estimated position of the needle provided by the previous needle model curve is assumed to be the needle artifact, and the position of its centroid determines the observed position of the needle in this image. The position of the needle base is appended to this list of needle coordinates, and the combined list is used as one of the inputs for the needle curve optimization.

4.2 Experiment

Several assumptions made to reduce the complexity of the experiment and facilitate needle tracking are listed below.

- A single beveled-tip clinical-style biopsy needle is to be inserted and tracked.

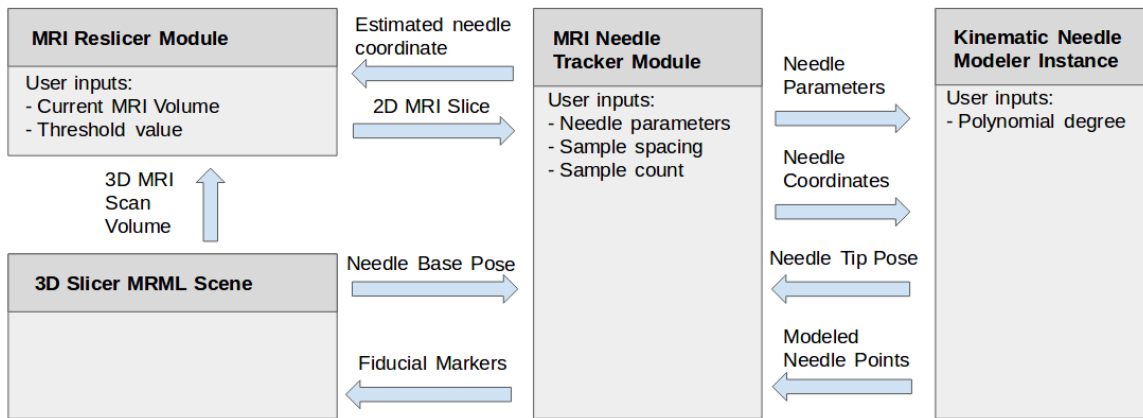


Figure 4.1: System architecture for needle detection and modeling from MRI data.

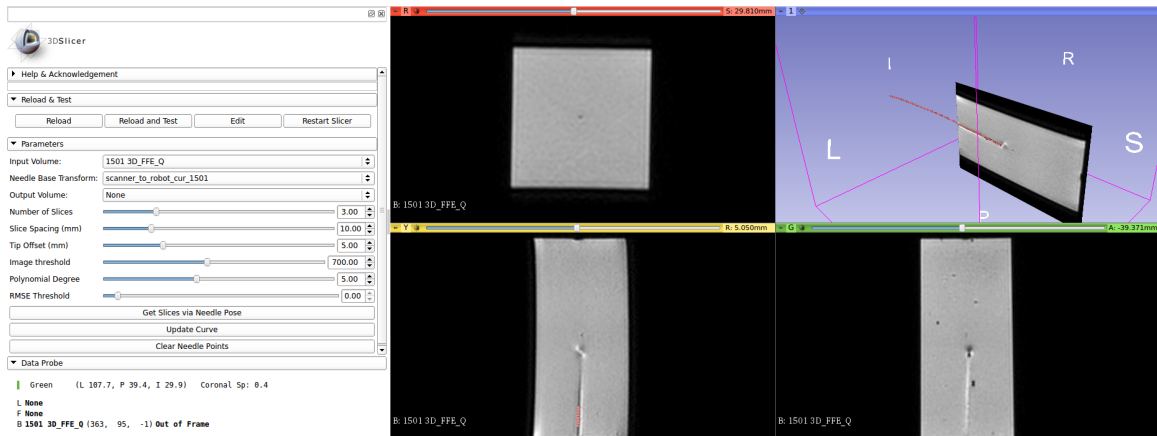


Figure 4.2: User interface for MRINeedleTipTracker 3D Slicer module.

- The initial vector of the needle is normal to the axial plane, and the actual pose of the needle base exactly matches the recorded pose.
- Only homogeneous gelatin tissue phantoms are considered. The problem of identifying the needle in the presence of anatomy or other clutter is not addressed.
- New MR data is acquired and transmitted instantaneously.

4.2.1 MRI Data Collection

The set of MRI volumes used in this experiment was captured in the 3T scanner at UMass Medical Center using a 3D Fast Field Echo protocol. The dimensions of each voxel are 0.4mm x 0.4mm x 0.5mm. The phantom used was made of agar gelatin. The needle was a 150mm stainless steel ($E = 200$ GPa) clinical-style biopsy needle with a beveled tip and a diameter of 2mm. Removable plastic spacers with a thickness of 5.95mm regulated the insertion distance. Two spacers were removed between scans, so the needle moves in increments of 11.9mm. Five scans were collected in total. The plastic alignment frame shown in Figure 4.3 kept the needle aligned along a known vector relative to the phantom. When used in conjunction the alignment frame and spacers allow the 6-DOF pose of the needle base to be calculated in each scan without the use of a Z-frame or external tracking equipment.

4.2.2 Needle Localization

Each volume was thresholded at intensity 1500 to isolate the needle artifact. The segmentation labelmap was exported and processed separately.

The MRI volumes for each insertion step were loaded in sequence and a linear transform was set to match the pose of the needle base at each step. The needle localization algorithm was run on each dataset in turn to generate an array of points representing the simulated needle.



Figure 4.3: Example tissue phantom with the needle alignment frame and biopsy needle.

4.3 Results

The baseline for the position of the needle shaft in the phantom was established by segmenting the needle artifact by intensity and computing the centroid of its cross section in every axial scan slice. Figure 4.4 shows the segmentation for the final step of the insertion, and Figure 4.5 shows the positions of the centroids in successive axial planes. The error for each model is computed as the difference between the centroid coordinate and the modeled coordinate in each slice.

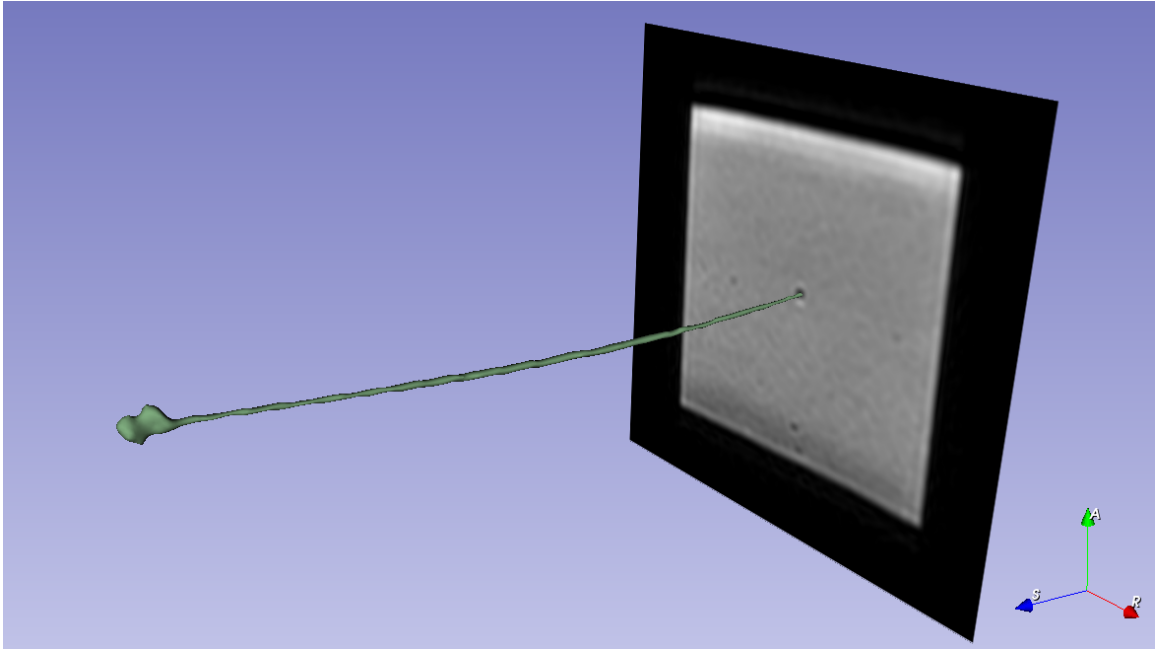


Figure 4.4: Segmentation of needle artifact generated by thresholding MRI volume.

4.3.1 Needle Localization at a Single Timestep

At the start of curve optimization using data from a single 3D scan in isolation the needle is assumed to be a vector with magnitude matching the length of the needle. The sampling locations are placed along the needle shaft starting from the needle tip and are offset from the estimated position of the tip by a user-configurable distance to avoid sampling points within the tip artifact.

Figure 4.6 shows the relative error using a 1st-, 3rd-, 5th-, and 7th-degree polynomials. In this experiment the tip offset $\delta = 5.0mm$, the sample spacing $d = 26.0mm$, and the number of observed slices $k = 3$.

Figure 4.7 shows the effect on error relative to baseline as the number of slices observed over the length of the needle is increased.

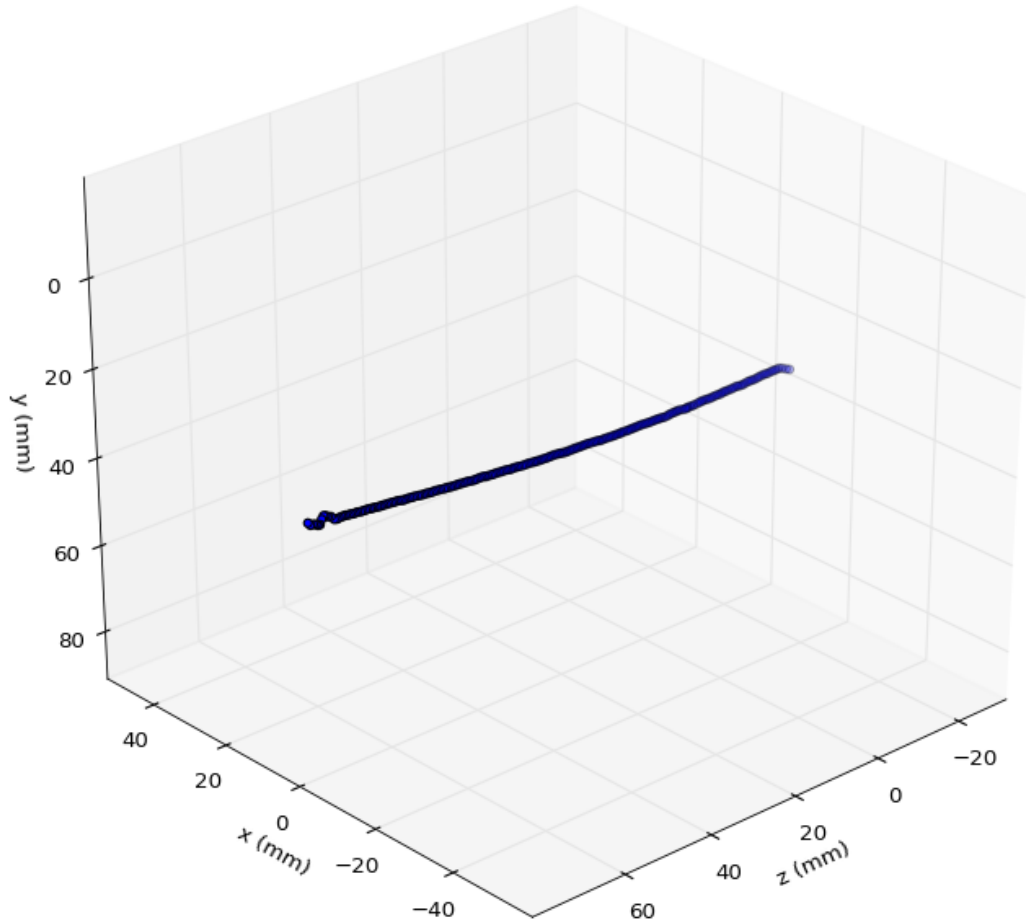


Figure 4.5: Baseline ground truth data, calculated from the centroids of the segmented artifact sectioned in the X-Y plane.

4.3.2 Needle Localization at Sequential Timesteps

Needle tracking in a sequence of images consists of repeated application of the method for an individual timestep described in 4.3.1. The optimized curve from the previous localization step is used as the initial estimate for the next localization step.

Figure 4.8 shows the positions of the scan planes and Figure 4.9 shows points along the optimized curve for each insertion interval. Figure 4.10 shows the magnitude of

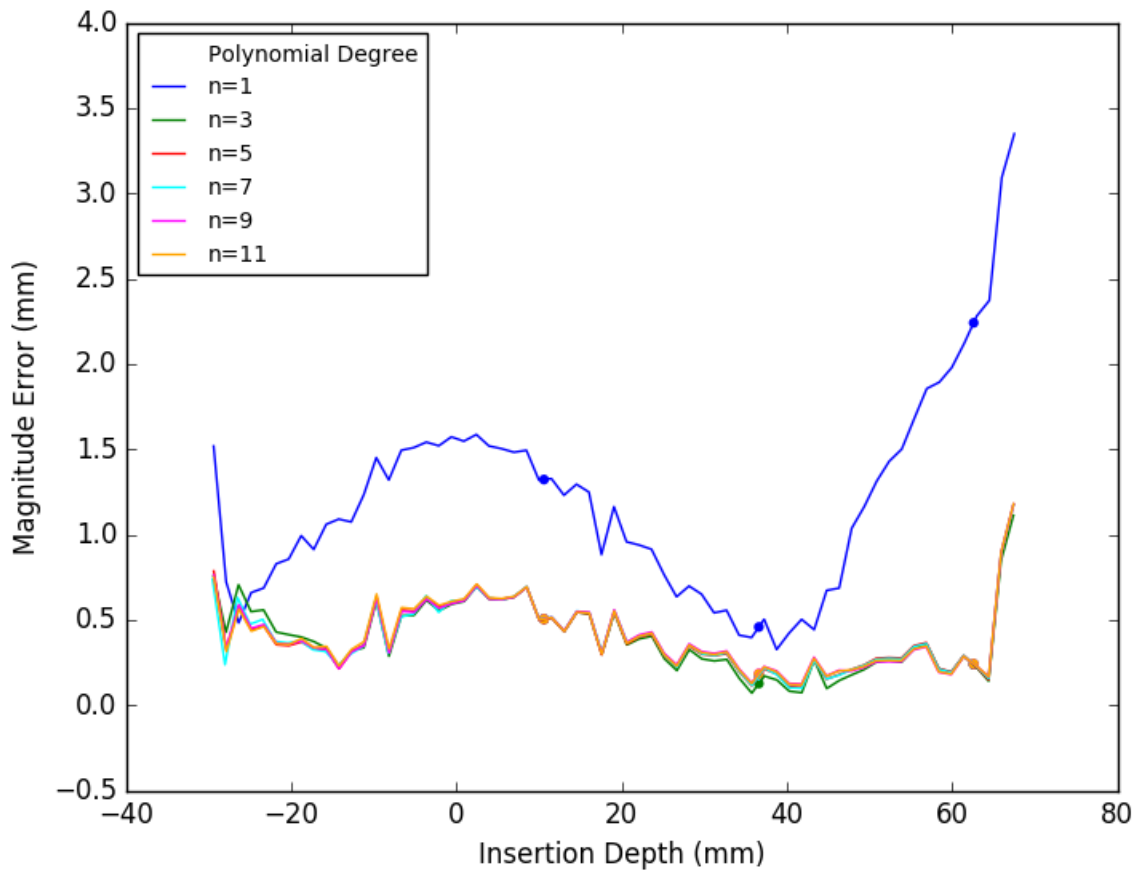


Figure 4.6: Magnitude of in-plane error over insertion for various degrees of polynomial. Markers indicate the positions of the slices on the needle curve. $d = 26.0mm$, $k = 3$, $\delta = 5.0mm$

error relative to the baseline for the optimized curve at each interval. Figure 4.11 shows the magnitude of error when the spacing between the slices is increased as the needle is inserted.

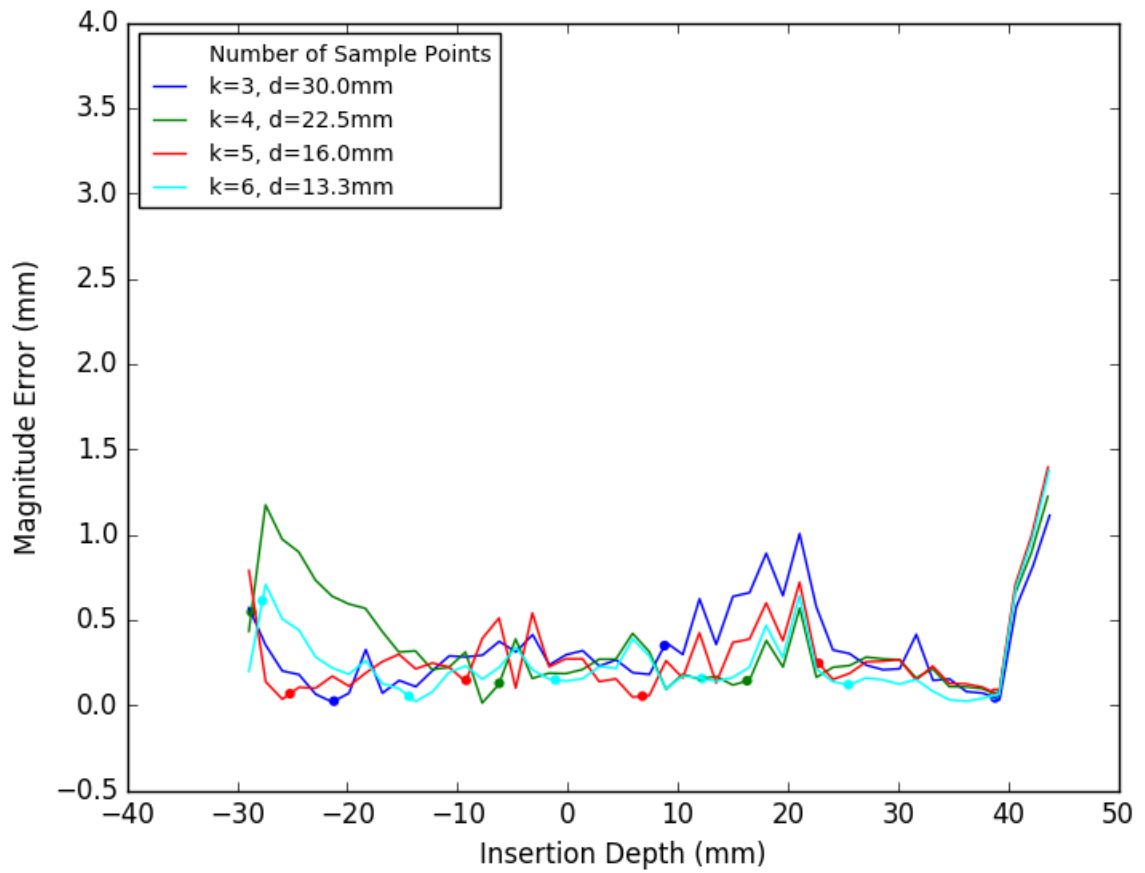


Figure 4.7: Magnitude of in-plane error over insertion for a variable number of sample points. Markers indicate slice positions. $n = 5$, $\delta = 5.0mm$

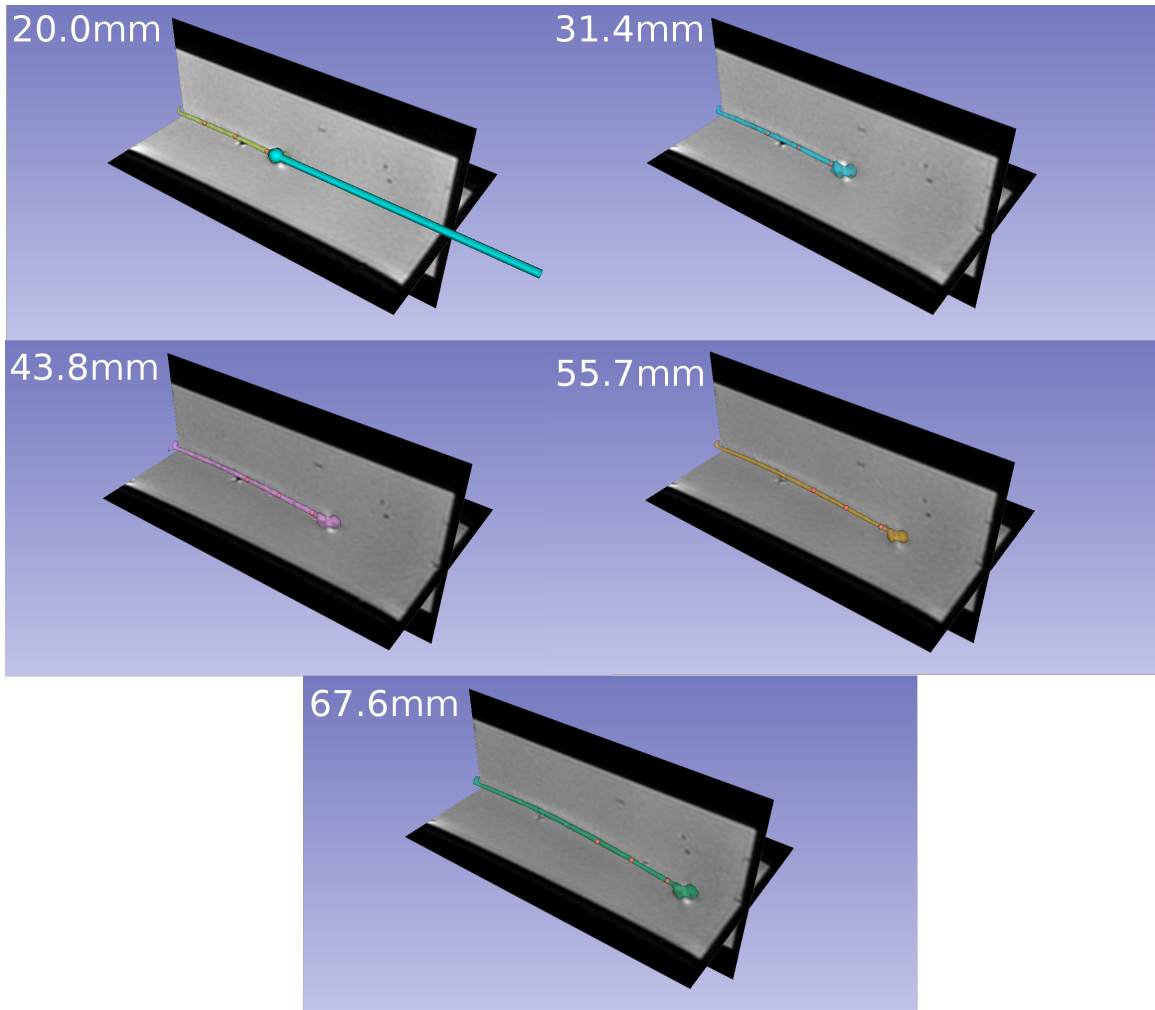


Figure 4.8: Positions of 2D scan planes at each insertion step, with segmented artifact.

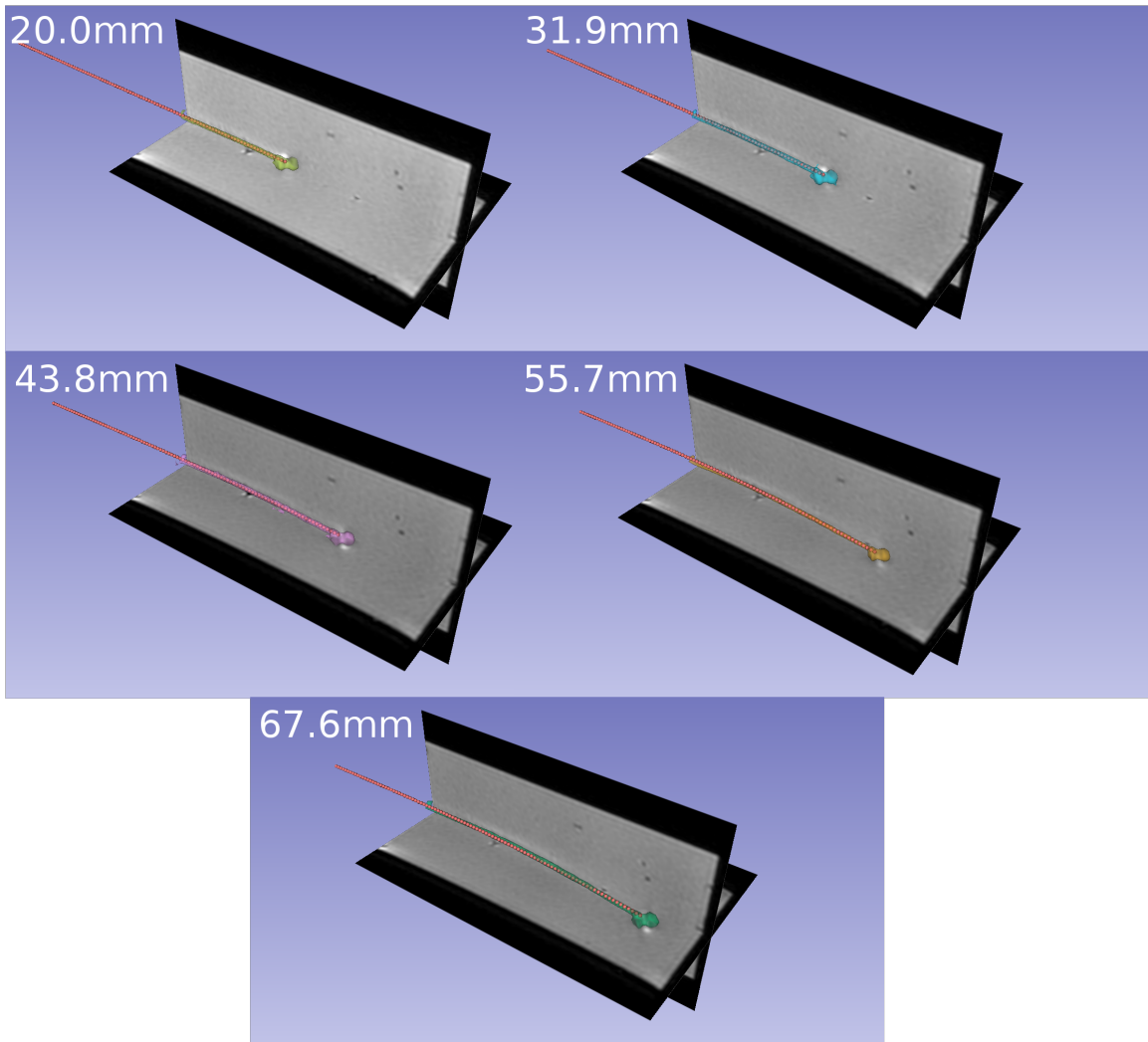


Figure 4.9: Modeled curve points at each insertion step, with segmented artifact.

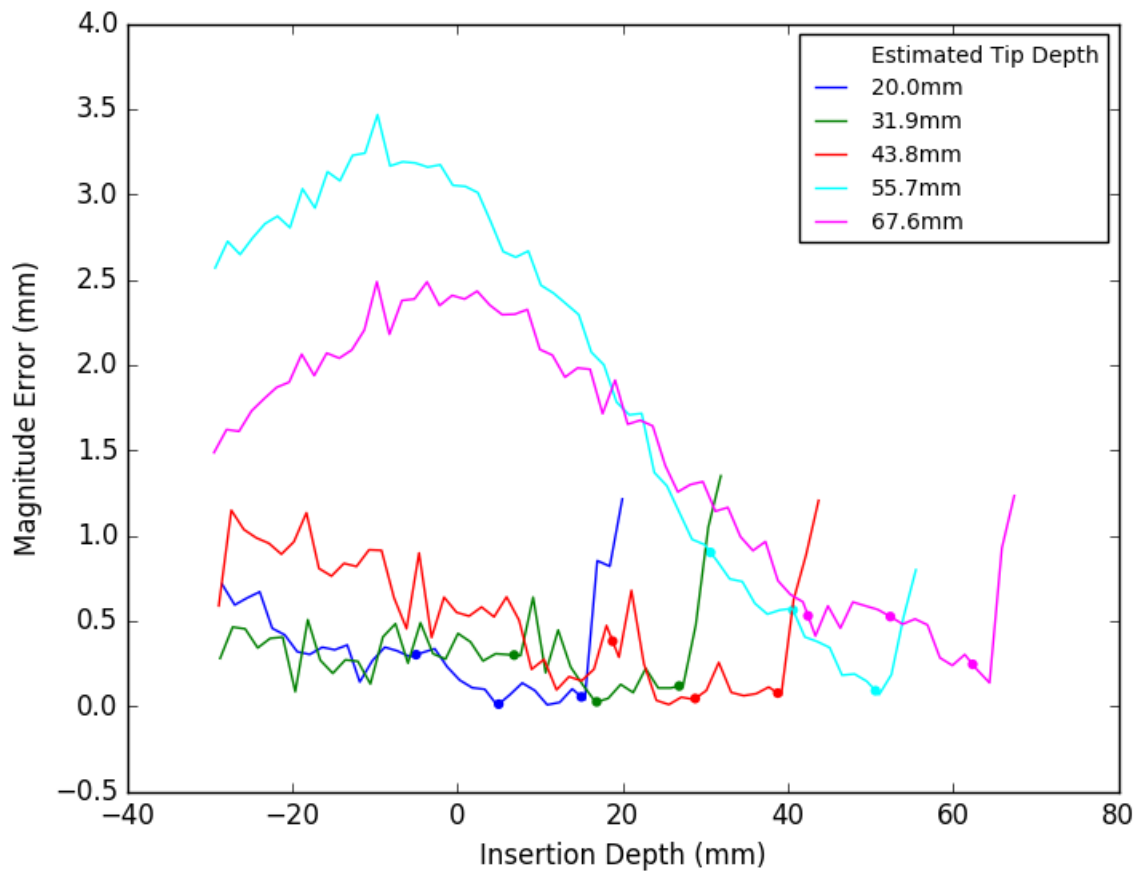


Figure 4.10: Magnitude of error between the needle model and the artifact centroid with fixed spacing between slices. Markers indicate slice positions. $d = 10mm$, $k = 3$, $\delta = 5mm$

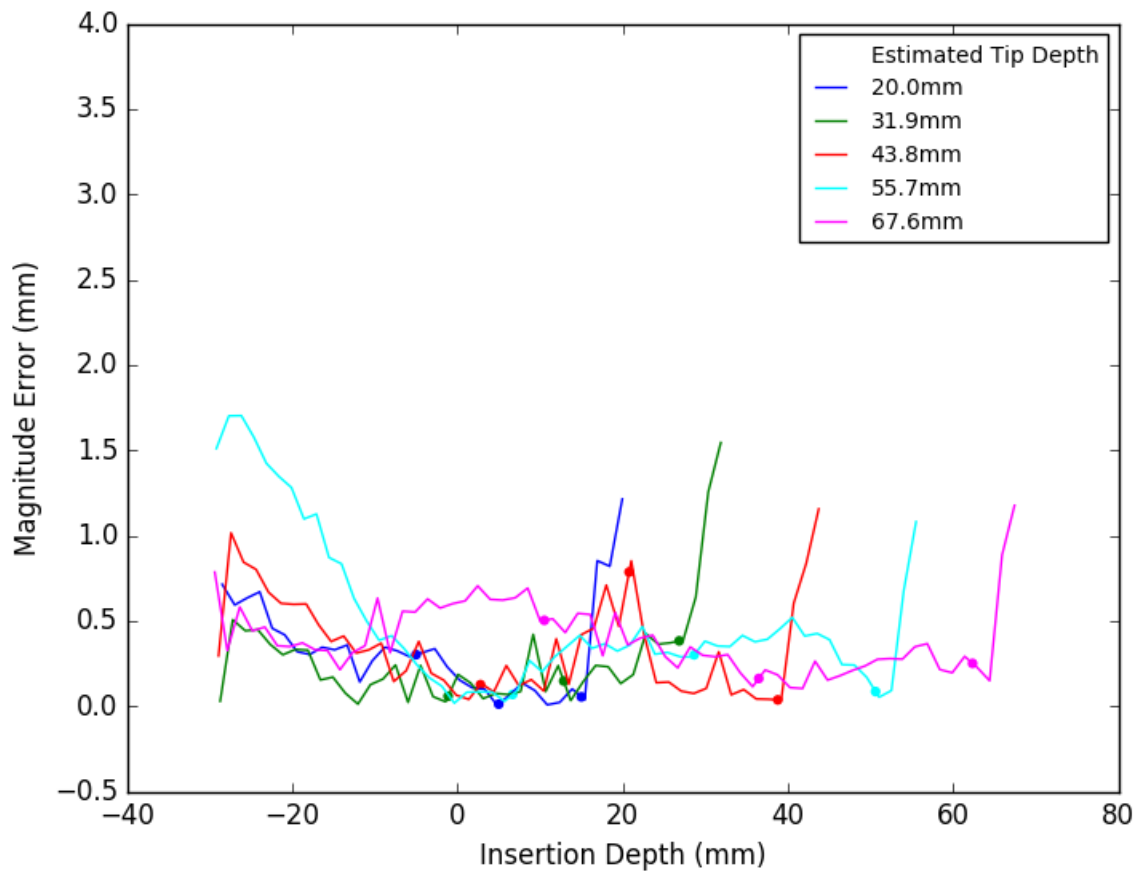


Figure 4.11: Magnitude of error between the needle model and the artifact centroid, where the spacing between each slice increases with insertion depth. Markers indicate slice positions. $d = 10mm + index_{step} * 4mm$, $k = 3$, $\delta = 5mm$

Chapter 5

Discussion and Conclusion

5.1 Discussion

5.1.1 MRI Experiment

The experimental results show that the key components of closed-loop model-guided needle localization all work in conjunction. The needle artifact centroids are all correctly identified by thresholding the image and identifying the region with the centroid closest to the estimated needle position in the scan. Needle cross-section identification finds the correct artifact even when other large non-needle artifacts are present.

The error relative to the artifact cross-section centroid outside the tip artifact region is less than 0.5mm, which is comparable to other work in needle localization in

US [34] and MRI [13]. The length constraint allows the needle curve to extend beyond the furthest sampled point into the tip artifact region, but the error is high in the tip artifact region because the artifact is lopsided and its centroid is not located on the needle shaft. This is a shortcoming in the baseline dataset and does not reflect the error relative to the actual position of the needle. Extending the dataset to include a CT scan at each needle insertion step would provide a superior baseline for the entire needle. Since the image of the needle in the CT scan would show the actual shape of the needle, a curve could be fit to this ground truth data to determine the polynomial degree n that best characterizes the shape of the needle.

The linear model exhibits significant error relative to the baseline and misrepresents the shape of the needle for a majority of its length. Choosing a polynomial with degree $n = 3$ reduces the error. For $k = 3$ sample points, choosing a higher-degree polynomial does not produce a further reduction in error because the polynomial is underconstrained with only $k = 3$ observations. Possible further reduction in error if a higher-degree polynomial is used and a greater number of points on the needle are observed should be explored further, especially if the needle bends in multiple directions throughout insertion.

Increasing the number of observation points along the length of the needle does not reduce the error relative to the baseline. The error in the model is high at base of the needle when the observation points are clustered near the needle tip, as shown in Figure 4.10, and low when the observations are evenly distributed along the observable

portion of the needle, as shown in Figure 4.11. This shows that sampling along the entire needle is important for accurate characterization of the needle.

In general, the concept of modeling the needle shape by sampling needle cross-sections in MRI is sound and could be extended for real-time applications.

5.1.2 Needle Model

The bending energy model is able to produce a good fit for the needle with very few sampled points. It does not over-fit, even when the small number of sample points would otherwise underconstrain the model. The curve between sample points approximately matches the actual position of the needle, and the estimated shape of the needle lies within the artifact region.

Optimization takes between 5 and 10 seconds (Lenovo ThinkPad P50, Intel Xeon CPU E3-1505M v5 @ 2.80GHz, 16 GB RAM) to converge to a solution depending on the constraints. The constraints on the needle length and the average error contribute to increased processing time. This is not an obstacle for an offline experiment, but it would present issues for real-time imaging. The choice of optimization algorithm likely has a significant impact on the total processing time. SLSQP performs the optimization sequentially, and an NLP optimizer designed to take advantage of parallel processing would probably complete the computation in a much shorter time.

The bending energy minimization approach is not guaranteed to provide a feasible solution for every possible combination of constraints and sample points. Even if a

solution is found, it is also not guaranteed to finish the optimization within a constant time, which might complicate integration into a real-time system.

5.2 Future Work

An important piece of follow-on work will be to demonstrate real-time tracking using live MR imaging. This will require implementation of a communication protocol that transmits scan plane poses to the MRI controller and listens for new image data. Precedent exists for controlling an MRI scanner in this way [8].

The time required to compute the needle curve optimization is very high and not currently suited for real-time operation. Possible solutions to reduce the computational load include reducing the number of numerical approximations in the optimization function, choosing a more efficient NLP optimization algorithm, and rewriting the needle modeling Python packages in C++.

5.3 Conclusion

This thesis presented a closed-loop model-based needle localization strategy agnostic to the imaging modality and independent of tissue mechanical properties. A simulated multi-step needle insertion in MRI was tracked, and the error between the estimated position of the needle shaft from the model and the measured position of the centroid of the needle artifact was comparable to previously-published needle lo-

calization approaches. The bending energy minimization approach produces accurate curve fits using a small number of images by also considering the kinematics of the insertion platform. While not extensively explored in this work, the parametric polynomial needle curve and the concept of planning scan planes using the curve could work for a very wide array of needle trajectories, including loops and other paths rarely explored in other literature.

References

- [1] J. G. R. Bomers, J. P. M. Sedelaar, J. O. Barentsz, and J. J. Fütterer, “MRI-Guided Interventions for the Treatment of Prostate Cancer,” *American Journal of Roentgenology*, vol. 199, no. 4, pp. 714–720, Oct. 2012.
- [2] S. Nath, Z. Chen, N. Yue, S. Trumppore, and R. Peschel, “Dosimetric effects of needle divergence in prostate seed implant using ^{125}I and ^{103}Pd radioactive seeds,” *Medical Physics*, vol. 27, no. 5, pp. 1058–1066, May 2000.
- [3] J. H. Youk, E.-K. Kim, M. J. Kim, J. Y. Lee, and K. K. Oh, “Missed breast cancers at US-guided core needle biopsy: How to reduce them,” *Radiographics: A Review Publication of the Radiological Society of North America, Inc*, vol. 27, no. 1, pp. 79–94, 2007 Jan-Feb.
- [4] J. Tokuda, K. Tuncali, I. Iordachita, S.-E. Song, A. Fedorov, S. Oguro, A. Lasso, F. M. Fennessy, C. M. Tempany, and N. Hata, “In-bore setup and Software for 3T MRI-guided Transperineal Prostate Biopsy,” *Physics in medicine and biology*, vol. 57, no. 18, pp. 5823–5840, Sep. 2012.
- [5] G. Onik, E. R. Cosman, T. H. Wells, H. I. Goldberg, A. A. Moss, P. Costello, R. A. Kane, W. I. Hoddick, and B. Demas, “CT-guided aspirations for the body: Comparison of hand guidance with stereotaxis,” *Radiology*, vol. 166, no. 2, pp. 389–394, Feb. 1988.
- [6] C. R. Weiss, S. G. Nour, and J. S. Lewin, “MR-guided biopsy: A review of current techniques and applications,” *Journal of Magnetic Resonance Imaging*, vol. 27, no. 2, pp. 311–325, Feb. 2008.
- [7] C. Menard, D. Iupati, J. Lee, A. Simeonov, J. Abed, J. Publicover, P. Chung, A. Bayley, C. Catton, M. Milosevic, R. Bristow, G. Morton, P. Warde, K. Brock,

- and M. Haider, “MRI and Biopsy Performance in Delineating Recurrent Tumor Boundaries after Radiotherapy for Prostate Cancer,” p. 1.
- [8] N. A. Patel, T. van Katwijk, G. Li, P. Moreira, W. Shang, S. Misra, and G. S. Fischer, “Closed-loop asymmetric-tip needle steering under continuous intraoperative MRI guidance,” in *2015 37th Annual International Conference of the IEEE Engineering in Medicine and Biology Society (EMBC)*, Aug. 2015, pp. 4869–4874.
- [9] G. J. Vrooijink, M. Abayazid, S. Patil, R. Alterovitz, and S. Misra, “Needle path planning and steering in a three-dimensional non-static environment using two-dimensional ultrasound images,” *The International Journal of Robotics Research*, vol. 33, no. 10, pp. 1361–1374, Sep. 2014.
- [10] “3D Slicer,” <https://www.slicer.org/>.
- [11] A. Fedorov, R. Beichel, J. Kalpathy-Cramer, J. Finet, J.-C. Fillion-Robin, S. Pujol, C. Bauer, D. Jennings, F. Fennessy, M. Sonka, J. Buatti, S. Aylward, J. V. Miller, S. Pieper, and R. Kikinis, “3D Slicer as an Image Computing Platform for the Quantitative Imaging Network,” *Magnetic resonance imaging*, vol. 30, no. 9, pp. 1323–1341, Nov. 2012.
- [12] J. S. Lewin, J. L. Duerk, V. R. Jain, C. A. Petersilge, C. P. Chao, and J. R. Haaga, “Needle localization in MR-guided biopsy and aspiration: Effects of field strength, sequence design, and magnetic field orientation.” *American Journal of Roentgenology*, vol. 166, no. 6, pp. 1337–1345, Jun. 1996.
- [13] S.-E. Song, N. B. Cho, I. Iordachita, P. Guion, G. Fichtinger, A. Kaushal, K. Camphausen, and L. L. Whitcomb, “Biopsy Needle Artifact Localization in MRI-guided Robotic Transrectal Prostate Intervention,” *IEEE transactions on bio-medical engineering*, vol. 59, no. 7, pp. 1902–1911, Jul. 2012.
- [14] S. Misra, K. Reed, B. Schafer, K. Ramesh, and A. Okamura, “Mechanics of Flexible Needles Robotically Steered through Soft Tissue,” *The International Journal of Robotics Research*, vol. 29, no. 13, pp. 1640–1660, Nov. 2010.

- [15] R. J. Webster, J. S. Kim, N. J. Cowan, G. S. Chirikjian, and A. M. Okamura, “Nonholonomic Modeling of Needle Steering,” *The International Journal of Robotics Research*, vol. 25, no. 5-6, pp. 509–525, May 2006.
- [16] N. J. Cowan, K. Goldberg, G. S. Chirikjian, G. Fichtinger, R. Alterovitz, K. B. Reed, V. Kallem, W. Park, S. Misra, and A. M. Okamura, “Robotic Needle Steering: Design, Modeling, Planning, and Image Guidance,” in *Surgical Robotics*. Springer, Boston, MA, 2011, pp. 557–582.
- [17] K. B. Reed, A. M. Okamura, and N. J. Cowan, “Modeling and Control of Needles With Torsional Friction,” *IEEE Transactions on Biomedical Engineering*, vol. 56, no. 12, pp. 2905–2916, Dec. 2009.
- [18] J. P. Swensen, M. Lin, A. M. Okamura, and N. J. Cowan, “Torsional Dynamics of Steerable Needles: Modeling and Fluoroscopic Guidance,” *IEEE Transactions on Biomedical Engineering*, vol. 61, no. 11, pp. 2707–2717, Nov. 2014.
- [19] O. Goksel, E. Dehghan, and S. E. Salcudean, “Modeling and simulation of flexible needles,” *Medical Engineering and Physics*, vol. 31, no. 9, pp. 1069–1078, Nov. 2009.
- [20] A. Chentanez, C. Ritchie, G. Hauser, and O. Shewchuk, “Interactive Simulation of Surgical Needle Insertion and Steering,” p. 10, 2009.
- [21] E. Dehghan, O. Goksel, and S. E. Salcudean, “A Comparison of Needle Bending Models,” in *Medical Image Computing and Computer-Assisted Intervention – MICCAI 2006*, ser. Lecture Notes in Computer Science. Springer, Berlin, Heidelberg, Oct. 2006, pp. 305–312.
- [22] A. C. Barnett, Y.-S. Lee, and J. Z. Moore, “Fracture Mechanics Model of Needle Cutting Tissue,” *Journal of Manufacturing Science and Engineering*, vol. 138, no. 1, pp. 011 005–011 005–8, Sep. 2015.
- [23] M. Abayazid, R. J. Roesthuis, R. Reilink, and S. Misra, “Integrating Deflection Models and Image Feedback for Real-Time Flexible Needle Steering,” *IEEE Transactions on Robotics*, vol. 29, no. 2, pp. 542–553, Apr. 2013.

- [24] R. J. Roesthuis, N. J. van de Berg, J. J. van den Dobbelsteen, and S. Misra, “Modeling and steering of a novel actuated-tip needle through a soft-tissue simulant using Fiber Bragg Grating sensors,” in *2015 IEEE International Conference on Robotics and Automation (ICRA)*, May 2015, pp. 2283–2289.
- [25] V. Duindam, J. Xu, R. Alterovitz, S. Sastry, and K. Goldberg, “Three-dimensional Motion Planning Algorithms for Steerable Needles Using Inverse Kinematics,” *The International Journal of Robotics Research*, vol. 29, no. 7, pp. 789–800, Jun. 2010.
- [26] S. P. DiMaio and S. E. Salcudean, “Needle insertion modeling and simulation,” *IEEE Transactions on Robotics and Automation*, vol. 19, no. 5, pp. 864–875, Oct. 2003.
- [27] D. Glozman and M. Shoham, “Image-Guided Robotic Flexible Needle Steering,” *IEEE Transactions on Robotics*, vol. 23, no. 3, pp. 459–467, Jun. 2007.
- [28] K. B. Reed, V. Kallem, R. Alterovitz, K. Goldberg, A. M. Okamura, and N. J. Cowan, “Integrated planning and image-guided control for planar needle steering,” in *2008 2nd IEEE RAS EMBS International Conference on Biomedical Robotics and Biomechatronics*, Oct. 2008, pp. 819–824.
- [29] P. J. Swaney, J. Burgner, H. B. Gilbert, and R. J. Webster, “A Flexure-Based Steerable Needle: High Curvature With Reduced Tissue Damage,” *IEEE Transactions on Biomedical Engineering*, vol. 60, no. 4, pp. 906–909, Apr. 2013.
- [30] R. J. Webster, J. M. Romano, and N. J. Cowan, “Mechanics of Precurved-Tube Continuum Robots,” *IEEE Transactions on Robotics*, vol. 25, no. 1, pp. 67–78, Feb. 2009.
- [31] D. C. Rucker, B. A. Jones, and R. J. W. III, “A Geometrically Exact Model for Externally Loaded Concentric-Tube Continuum Robots,” *IEEE Transactions on Robotics*, vol. 26, no. 5, pp. 769–780, Oct. 2010.
- [32] P. E. Dupont, J. Lock, B. Itkowitz, and E. Butler, “Design and Control of Concentric-Tube Robots,” *IEEE transactions on robotics : a publication of the IEEE Robotics and Automation Society*, vol. 26, no. 2, pp. 209–225, Apr. 2010.

- [33] J. Carriere, C. Rossa, N. Usmani, R. Sloboda, and M. Tavakoli, “Needle shape estimation in soft tissue based on partial ultrasound image observation,” in *2015 IEEE International Conference on Robotics and Automation (ICRA)*, May 2015, pp. 2277–2282.
- [34] C. Rossa, M. Khadem, R. Sloboda, N. Usmani, and M. Tavakoli, “Adaptive Quasi-Static Modelling of Needle Deflection During Steering in Soft Tissue,” *IEEE Robotics and Automation Letters*, vol. 1, no. 2, pp. 916–923, Jul. 2016.
- [35] G. Pernelle, A. Mehrtash, L. Barber, A. Damato, W. Wang, R. T. Seethamraju, E. Schmidt, R. Cormack, W. Wells, A. Viswanathan, and T. Kapur, “Validation of Catheter Segmentation for MR-guided Gynecologic Cancer Brachytherapy,” *Medical image computing and computer-assisted intervention : MICCAI ... International Conference on Medical Image Computing and Computer-Assisted Intervention*, vol. 16, no. 0 3, pp. 380–387, 2013.
- [36] F. Zijlstra, J. G. Bouwman, I. Braškutè, M. A. Viergever, and P. R. Seevinck, “Fast Fourier-based simulation of off-resonance artifacts in steady-state gradient echo MRI applied to metal object localization,” *Magnetic Resonance in Medicine*, vol. 78, no. 5, pp. 2035–2041, Nov. 2017.
- [37] R. J. Roesthuis, M. Kemp, J. J. van den Dobbelen, and S. Misra, “Three-Dimensional Needle Shape Reconstruction Using an Array of Fiber Bragg Grating Sensors,” *IEEE/ASME Transactions on Mechatronics*, vol. 19, no. 4, pp. 1115–1126, Aug. 2014.
- [38] S. Patil, J. Burgner, R. J. Webster, and R. Alterovitz, “Needle Steering in 3-D Via Rapid Replanning,” *IEEE transactions on robotics : a publication of the IEEE Robotics and Automation Society*, vol. 30, no. 4, pp. 853–864, Aug. 2014.
- [39] W. Wang, C. L. Dumoulin, A. N. Viswanathan, Z. T. H. Tse, A. Mehrtash, W. Loew, I. Norton, J. Tokuda, R. T. Seethamraju, T. Kapur, A. L. Damato, R. A. Cormack, and E. J. Schmidt, “Real-time active MR-tracking of metallic stylets in MR-guided radiation therapy,” *Magnetic resonance in medicine : official journal of the Society of Magnetic Resonance in Medicine / Society of Magnetic Resonance in Medicine*, vol. 73, no. 5, pp. 1803–1811, May 2015.

- [40] R. J. Roesthuis, M. Abayazid, and S. Misra, “Mechanics-based model for predicting in-plane needle deflection with multiple bends,” in *2012 4th IEEE RAS EMBS International Conference on Biomedical Robotics and Biomechatronics (BioRob)*, Jun. 2012, pp. 69–74.
- [41] D. Kraft, *A Software Package for Sequential Quadratic Programming*. Köln: DFVLR, 1988, open Library ID: OL18926873M.